



2 Assessment of the Finite VolumE Sea Ice Ocean Model 3 (FESOM2.0), Part I: Description of selected key model 4 elements and comparison to its predecessor version

5 Patrick Scholz¹, Dmitry Sidorenko¹, Ozgur Gurses¹, Sergey Danilov^{1,2}, Nikolay Koldunov^{1,3}, Qiang
6 Wang¹, Dmitry Sein¹, Margarita Smolentseva¹, Natalja Rakowsky¹, Thomas Jung^{1,4}

7 ¹ Alfred Wegener Institute Helmholtz Center for Polar and Marine Research (AWI), Bremerhaven, Germany

8 ² Jacobs University Bremen, Department of Mathematics & Logistics, Bremen, Germany

9 ³ MARUM-Center for Marine Environmental Sciences, Bremen, Germany

10 ⁴ University of Bremen, Department of Physics and Electrical Engineering, Bremen, Germany

11

12
13
14 *Correspondence to:* Patrick Scholz (Patrick.Scholz@awi.de)

15 **Abstract.** The evaluation and model element description of the second version of the unstructured-mesh Finite-volumE
16 Sea ice–Ocean circulation Model (FESOM2.0) is presented. The model sensitivity to arbitrary Lagrangian Eulerian
17 (ALE) linear and nonlinear free surface formulation, Gent McWilliams eddy parameterisation, isoneutral Redi diffusion
18 and different vertical mixing schemes is documented. The hydrographic biases, large scale circulation, numerical
19 performance and scalability of FESOM2.0 are compared with its predecessor FESOM1.4. FESOM2.0 shows biases
20 with a magnitude comparable to FESOM1.4 and it simulates a more realistic AMOC. Compared to its predecessor
21 FESOM2.0 provides clearly defined fluxes and a three times higher throughput in terms of simulated years per day
22 (SYPD). It is thus the first mature global unstructured-mesh ocean model with computational efficiency comparable to
23 state-of-the-art structured-mesh ocean models. Other key elements of the model and new development will be described
24 in following-up papers.

25 1 Introduction

26 Ocean general circulation models that work on unstructured meshes have been established in the coastal ocean
27 modeling community a long time ago, offering the multi-resolution functionality without taking the effort of grid
28 nesting techniques as required by regular-grid models. Unstructured meshes provide an opportunity to increase spatial
29 resolution in dynamically active regions to locally resolve small scale processes (for example, mesoscale eddies) or
30 geometric features instead of parameterizing their effects while keeping a coarse resolution elsewhere.

31 In recent years, unstructured-mesh models have become well-established tools to study global ocean and climate. The
32 Finite Element Sea Ice Ocean Model version 1.4 (FESOM1.4, Wang et al., 2014), the first mature global multi-
33 resolution unstructured-mesh model developed for simulating the global ocean general circulation for climate research,
34 set a milestone in the development of new generation ocean models. The success of FESOM1.4 was based on the
35 experience gained during the development of its predecessor versions (Danilov et al., 2004; Wang et al., 2008;
36 Timmermann et al., 2009). The studies performed with FESOM1.4 proved the value of global multi-resolution
37 unstructured meshes for simulating local ocean dynamics (Wang et al., 2016, 2018; Wekerle et al., 2017) and exploring
38 their global effects (Rackow et al., 2016; Scholz et al., 2014; Sein et al., 2018; Sidorenko et al., 2011, 2018) with



40 acceptable computational costs. In the meantime, other global unstructured-mesh models have emerged, with promising
41 progress in their development (Ringler et al., 2013; Korn et al., 2017).

42 Although FESOM1.4 was optimized to have throughput (in terms of simulated years per day) comparable to structured-
43 grid models in massively parallel applications, it requires more than three times the computational resources (in terms
44 of CPU time per grid point per time step) of a typical ocean model using structured meshes (Bjastoch et al., 2018). In
45 the recent years, when global mesoscale eddy resolving configurations came to the focus of climate research, the limits
46 of FESOM1.4 due to its high demands in terms of computational resources became more and more obvious (Sein et al.,
47 2017, 2018). This motivated the development of the new model version FESOM2.0 (Danilov et al., 2017).

48 FESOM2.0 builds on the framework of its predecessor FESOM1.4, using its sea-ice component FESIM (Danilov et al.,
49 2015), general user interface and code structure. Both model versions work on unstructured triangular meshes, although
50 the horizontal location of quantities and vertical discretization are different. FESOM2.0 uses a B-Grid like horizontal
51 discretization, where scalar values are located at triangle vertices and horizontal velocities are located at triangle
52 centroids, while in FESOM1.4 all quantities were located at the vertices. In the vertical, FESOM2.0 uses a prismatic
53 discretization where all the variables, except the vertical velocity, are located at mid-depth levels, while in FESOM1.4
54 each triangular prism is split into three tetrahedral elements and variables are located at full depth levels. In addition, in
55 FESOM2.0 the interfaces for data input and output are further modularized and generalized to facilitate massively
56 parallel applications.

The new numerical core of FESOM2.0 is based on the finite-volume method (Danilov et al., 2017). Its boost in
57 numerical efficiency comes largely from the more efficient data structure, that is, the use of two-dimensional storage for
58 three-dimensional variables. Due to the use of prismatic elements and vertical mesh alignment the horizontal
59 neighborhood pattern is preserved in the vertical. In FESOM1.4, three-dimensional variables are stored as one-
60 dimensional arrays, which requires more fetching time. More importantly, the vertices of tetrahedral elements and
61 derivatives on these elements need to be assessed for each tetrahedron separately, thus resulting in lower model
62 efficiency. Other major advantages of using finite-volumes are the clearly defined fluxes through the faces of the
63 control volume and the availability of various transport algorithms, whose choice was very limited for the continuous
64 Galerkin linear discretization of FESOM1.4 (Danilov et al., 2017). Arbitrary Lagrangian Eulerian (ALE; Ringler et al.,
65 2013; White et al., 2008; Danilov et al., 2017) vertical coordinates became an essential part of the numerical core of
66 FESOM2.0. In principle, ALE allows to utilize plenty of different vertical discretizations like geopotential, terrain-
67 following and hybrid coordinates as well as the usage of a linear free- or full free surface and generalized vertical layer
68 displacement within the same code.

70 After the release of FESOM2.0 (Danilov et al., 2017), substantial efforts have been devoted into the improvement of the
71 model parameterizations, adding different options of numerical and physical schemes, assessing and tuning the model
72 using a few standard FESOM configurations. The model development efforts for this model version will continue in the
73 future. This paper is the first in a series of publications that documents part of the progress made so far.

74 The motivation of the paper is twofold. First, we describe a number of key elements of the model that were added or
75 adjusted recently. We focus on the linear free and full free surface treatment, the effect of eddy stirring (Gent
76 McWilliams parameterization) and Redi diffusion, as well as the effect of different diapycnal mixing schemes on the
77 modeled ocean state. Second, a comparison between FESOM1.4 and the latest tuned version of FESOM2.0 is presented,
78 considering hydrography, meridional overturning circulation, scalability and mesh applicability. All simulations for



describing the model elements and comparing the model versions are carried out on a relatively coarse reference mesh,
80 while the simulations for the scalability test are performed on a medium sized mesh.

Our planned upcoming model development and assessment papers will deal with the following aspects: the performance
82 and influence of horizontal and vertical advection schemes of different orders as well as the flux corrected transport
(FCT) limiter on the state of the general ocean circulation, the effect of split explicit-implicit vertical advection
84 (Shchepetkin, 2015) in our model discretization, the effect of partial bottom cells and floating sea-ice, the
implementation of CVMIX and the new vertical mixing protocol IDEMIX (Olbers et al., 2017; Eden et al., 2017;
86 Pollman et al., 2017), the influence of different schemes for background diffusivities, the testing of different surface
forcing reanalysis data sets in FESOM2.0 and their associated climatological biases, and the implementation of terrain
88 following coordinates using vanishing quasi sigma coordinates.

90 The paper is structured as follows: In Section 2 we will describe the mesh configurations used in the simulations. The
description of key model elements and comparison between two model versions are presented in Section 3 and 4,
92 respectively. A summary is given in Section 5.

94 **2 Model configurations**

For the general evaluation of FESOM2.0 and the comparison between FESOM1.4 and FESOM2.0 we use a relatively-
96 coarse resolution reference mesh consisting of ~ 0.13 M surface vertices (Fig. 1 left). The mesh has a nominal resolution
of 1° in most parts of the global ocean, except north of 50°N where resolution is set to ~ 25 km, and in the equatorial
98 belt where resolution is increased to $1/3^\circ$. The resolution in the coastal regions is also slightly increased. The mesh has
48 unevenly distributed layers, with a top layer of 5 m, increasing stepwise to 250 m towards the bottom. The same
100 mesh has already been used in a variety of studies carried out with FESOM1.4, such as in the model intercomparison
project of the Coordinated Ocean Ice Reference Experiment - Phase II (CORE2), which proved that FESOM1.4
102 performs well compared to structured-mesh ocean models (see, e.g., Wang, 2016b, and other papers of the same virtual
issue).

104 The computational performance and scaling property estimations of FESOM2.0 and FESOM1.4 in section 4 are
conducted on an medium size mesh (Fig. 1 right, 0.64 M surface vertices) that shares the same resolution with the
106 reference mesh, except for the Arctic Ocean (including the Arctic gateways) and Bering Sea, where the resolution is
refined to ~ 4.5 km and ~ 10 km, respectively. All model setups are initialised with the Polar Science Center
108 Hydrographic winter Climatology (PHC3.0, updated from Steele et al., 2001) and forced by the CORE interannually
varying atmospheric forcing fields (Large and Yeager, 2009) for the period 1948-2009.

110

3 Model elements: Options and sensitivity studies

112 **3.1 Linear-free and full-free surface formulation**

FESOM1.4 supports two options for the free surface formulation. One option is the linear free surface whereby the sea



114 surface height equation is solved assuming a fixed mesh for tracer and momentum and consequently tracers cannot be
115 diluted or concentrated by ocean volume changes. With this option, to account for the impact of surface freshwater
116 fluxes on salinity, a virtual salt flux is added to the salinity equation through the surface boundary condition. Although
117 the formulation of a virtual salt flux mimics the effects of surface freshwater flux on the surface salinity, it has the
118 potential to change local salinity with certain biases and affect model integrity on long time scales (Wang et al., 2014).
119 This leads to the fact that modern ocean climate models, like the ones used in Danabasoglu et al. (2014), start to
120 abandon the fixed volume formulation in favor of a full free surface formalism. This option was also implemented in
121 FESOM1.4 but not widely used. The full free surface formulation in FESOM1.4 uses the arbitrary Lagrangian Eulerian
122 (ALE) framework in a finite-element sense where, due to costly updates of matrices and derivatives, only the surface
123 grid points are allowed to move (Wang et al., 2014).

124 The ALE vertical coordinate formulation is also used in FESOM2.0, but in a finite-volume sense (see Donea and
125 Huerta-Casas, 2003; Ringler et al. 2013; Adcroft and Hallberg, 2006; Danilov et al., 2017). It ensures a similar
126 functionality between FESOM1.4 and FESOM2.0 with respect to geopotential and terrain following coordinates and
127 linear and full free surface formulation. In FESOM2.0, the ALE formalism became an essential and elementary
128 integrated part of the numerical core, unlike in FESOM1.4 where it was only an additional feature to allow the surface
129 to move in the full free surface formulation. FESOM2.0 also offers the possibility to move all vertical layers, which
130 becomes a more frequently used option, since the associated computational cost in FESOM2.0 is strongly reduced
131 compared to FESOM1.4.

132 The adaptations that are made to the numerical code of FESOM2.0 in the course of the ALE implementation are
133 discussed in detail in Danilov et al. (2017). The main part of the ALE implementation is to introduce the thickness of
134 model ocean layers as an additional 3D variable that is allowed to vary horizontally in space and time. Thus, the ALE
135 approach in FESOM2.0 not only allows one to relatively easily implement different vertical discretizations by manually
136 assigning different initial layer thicknesses, but also supports options of varying vertical grids in time, including the full
137 nonlinear free surface option and isopycnal-following meshes. This means that the vertical grid can be fully Eulerian,
138 fully Lagrangian or something in between (see also Peterson et al., 2015).

For the linear free surface (hereafter called *linfs*) option in FESOM2.0, the 3D layer thicknesses are fixed in time and
140 the bottom to top volume of each vertical grid cell is kept constant during the simulation. This requires, like in
141 FESOM1.4, the introduction of a virtual salinity flux as an additional surface boundary condition in the salinity
142 equation to account for diluting and concentrating effects on salinity through surface freshwater fluxes (rain,
143 evaporation, river runoff, freshwater fluxes from ice melting/freezing).

144 In the full nonlinear free surface option, the total water column thickness is allowed to vary over time following the
145 change in sea surface height (SSH). Fresh-water fluxes can be directly applied to the surface layer thicknesses of the
146 thickness equation, which then modifies the surface salinity by changing the volume of the upper grid cells. The ocean
147 heat content change associated with surface water fluxes is added to the ocean temperature equation as the surface
148 boundary condition. For the full free surface case in FESOM2.0 we distinguish between two options. The first one is
149 called *zlevel*, where only the thickness of the surface layer is varied following the change of SSH, while all other layers
150 are kept fixed (Adcroft and Campin, 2004; Petersen et al., 2015; Danilov et al., 2017). This is equivalent to the only full
151 free surface option available in FESOM1.4. The second option is called *zstar*, where the total change in SSH is
152 distributed equally over all layers, except the layer that touches the bottom. This allows all layers above the bottom



154 layer to move vertically with time. In this case each layer only moves by a fraction of the total change of water column
155 thickness. Since in zlevel option the upper layer thickness can be altered more than in zstar case it is recommended to
156 use zstar in the full free surface formulation for the sake of stability.

157 In order to understand the effect of the linear free surface and the two full free surface options onto the simulated ocean
158 state, three model simulations were conducted using the linfs, zlevel and zstar configurations. Fig. 2 compares the
159 temperature anomalies of zlevel and zstar with respect to linfs (1st. and 2nd. column) and the temperature difference
160 between zlevel and zstar itself (3rd. column, zstar minus zlevel) over three different depth ranges. All presented model
161 results are averaged over the same time period 1998-2007 as in Danilov et al. (2017) to emphasize the improvements
162 that have been achieved and to keep the here presents results qualitatively comparable to the results shown there.

163 The overall patterns of temperature anomalies of zlevel and zstar with respect to linfs are very similar for all three depth
164 ranges, since the difference between zlevel and zstar is smaller by nearly one order of magnitude. Compared to linfs
165 both, zlevel and zstar show a strong warm signal along the pathway of the Gulf Stream (GS) together with cooling
166 anomalies in the North Atlantic subpolar gyre (along the pathway of the North Atlantic Current (NAC) and in Irminger
167 and Labrador Seas) that reach from the surface to the depth range of 500-1000m. Furthermore, the intermediate and
168 deeper depth ranges reveal slight warming anomalies in the Arctic Ocean (AO) and in the equatorial and South Atlantic,
and slight cooling anomalies in the equatorial and South Pacific and Indian Ocean.

169 The direct comparison between zlevel and zstar (Fig. 2, third column) shows that zstar in the surface and intermediate
170 depth ranges is warmer by up to 0.1°C in the tropics and subtropics and in parts of the North Atlantic, but colder along
171 the pathway of the GS, NAC and in the intermediate and deeper depth ranges of the Arctic Ocean. Overall, the
172 temperature difference between the two full free surface cases is much smaller than that caused by using the linear free
173 surface.

174 Fig. 3 presents the same comparison as Fig. 2 but for salinity. The salinity of zlevel and zstar (Fig. 3, first and second
175 column) shows nearly the same anomalies with respect to linfs. Both, zlevel and zstar indicate an overall freshening in
176 the Pacific, North Atlantic and Indian Ocean through all three considered depth ranges. They also show salinification of
177 up to 0.3 psu along the pathway of the GS and NAC, and slight salinification in the equatorial and South Atlantic at the
178 surface and intermediate depth, as well as in the Arctic Ocean in the intermediate depth range. The significant biases in
179 the coastal pathway of the GS between zlevel and zstar with respect to linfs originate from the fact that under zlevel and
180 zstar the boundary currents are stronger confined to the coast (not shown), which affects the detachment and the
181 eastward spread of the GS and thus the further northward heat and salt transport by the NAC and causes a cold and
182 fresh bias in the Irminger Sea. However for the deep ocean >1000m (not shown), zlevel and zstar indicate an overall
183 slight salinification bias. The direct comparison of the salinity between zlevel and zstar (zstar-zlevel, Fig. 3 third
184 column) indicates major differences for the surface and intermediate depth ranges of the Arctic Ocean and along the
185 pathway of the NAC. The same as for temperature, the difference in salinity between the two free surface options is
186 much smaller than the difference between any of these and the linear free surface option.

187 In FESOM2.0 we tried two different ways of computing the mixed layer depth (MLD). One way follows the definition
188 of Monterey and Levitus, (1997) who compute MLD as the depth at which the density over depth differs by 0.125
189 sigma units from the surface density (Griffies et al., 2009). This MLD definition was also supported in FESOM1.4
190 (hereafter referred as MLD1). The other way follows the definition of Large et al. (1997), who suggest to compute



192 MLD as the shallowest depth where the vertical derivative of buoyancy is equal to a local critical buoyancy gradient
(Griffies et al., 2009) (hereafter referred as MLD2). Both definitions reveal large MLD differences especially in the
194 Southern Ocean. The first column in Fig. 4 shows the northern hemispheric March (upper row) and southern
hemispheric September (lower row) mean MLD averaged over the period 1998-2007 in the linfs option. The main plots
196 show the absolute and anomalous values of MLD1, while the small insets show the absolute values of MLD2. In the
northern hemisphere the March MLD1 indicates mixed depths of up to 3000 m in the entire Labrador Sea together with
198 a weaker MLD1 in parts of Irminger Sea and central GIN Sea, while MLD2 shows only a maximum of ~1700 m in the
northwest Labrador Sea with weaker a MLD of ~900 m in the Irminger Sea and ~450 m along the pathway of the
200 Norwegian boundary current. The southern hemispheric September MLD1 (linfs) shows high values for the entire
Weddel Sea, while the MLD2 indicates no large values in the entire Southern Ocean.

202 The differences in MLD1 between zlevel and zstar with respect to linfs (Fig. 4, second and third columns) show for
March and September almost identical patterns, with a reduction of the March MLD along the pathway of the Labrador
204 Current, in the southern Labrador Sea and in the central GIN Sea, accompanied by a gain in MLD in the western
Irminger Sea. The difference in September MLD1 between zlevel and zstar with respect to linfs, shows a strong
206 reduction and gain in the MLD for the northwestern and southeastern Weddel Sea, respectively. The direct MLD
comparison between zlevel and zstar (Fig. 4 fourth column, zstar minus zlevel) reveals for March and September local
208 heterogeneous anomaly pattern with a maximum amplitude of ~300 m and with a tendency to a slightly increased zstar
March and September MLD, when compared to zlevel. Inspecting the spread in MLD patterns from these simulations
210 we conclude that (1) as a consequence of different stratification strength the MLD map is sensitive to the way of how it
is computed. The largest discrepancies between two diagnostics used in this paper are in the SO. (2) Through altering
212 the stratification, different model options can affect various MLD diagnostics in different ways.

214 To demonstrate the effect of the linear free surface and full free surface on large scale ocean circulation, we show the
streamfunction of the meridional overturning circulation (MOC) for the global- (GMOC, upper row), Atlantic- (AMOC,
216 middle row) and Indo-Pacific Meridional Overturning Circulation (PMOC, lower row) in Fig. 5 for the three
simulations. All three cases show similar strength in the circulation of the Antarctic Bottom Water (AABW) of the
218 GMOC, AMOC and PMOC, but slight differences in the shape of the AABW cell. For the GMOC, linfs obtains a
stronger north Atlantic deep water (NADW) upper circulation cell with maximum transport of ~15 Sv at ~40°N, while
220 zlevel and zstar have maximum transport of ~12.5 Sv at 40°N. The GMOC AABW cell extends more northward in linfs
compared to zlevel and zstar. The strength and structure of the southern ocean Deacon cell (Kuhlbrodt et al.,
222 2007) looks fairly the same for all three cases. All three simulations show no connection of the AABW cell to the upper
circumpolar deep water (UCDW). The NADW cell of the AMOC has a maximum strength of 15 Sv and 12 Sv for linfs
224 and the two full free surface cases, respectively. For the AABW cell of the AMOC, the three simulations have similar
strength of ~-2 Sv. However, linfs has its maxima located north of 35°N, while zlevel and zstar have their maxima
226 located south of 20°N. In the North Pacific, the circulation of the PMOC bottom cell is stronger in the linfs case, which
has a larger vertical extent than zlevel and zstar. In the latter cases the AABW cell is confined below 2000 m depth. For
228 all the three diagnosed meridional overturning circulation streamfunctions (GMOC, AMOC and PMOC), the two full-
free surface cases show negligible difference.

230 Overall, the sensitivity tests indicate that the differences in ocean hydrography and circulation between using linear free



232 surface and full free surface options are not negligible. However, the differences are less significant than those between
233 different ocean models as shown in the CORE-II model intercomparison project (e.g., Danabasoglu et al., 2014), and
234 also less significant than the differences associated with tuning other model parameters as presented in the following
subsections.

236 3.2 Parameterizations of eddy stirring and mixing

237 With the increase of computational resources the ocean modelling community aims at resolving the mesoscale eddies in
238 the ocean through increasing resolution of computational grids. As discussed in Hallberg (2013), the resolution of two
239 grid points per Rossby radius of deformation should be the target in the near future. Considering that the Rossby radius
240 can be as small as a few kilometer in high latitudes and even less than 1km in high-latitude shelf regions, the size of the
241 desired computational grid to resolve mesoscales globally is far larger than those which are currently employed in
242 climate models. Moreover, there are indications that in some regions the threshold of two grid points per Rossby radius
243 marks only the lower boundary of the desired grid resolution (Sein et al., 2017). Therefore, parameterizations for
244 mesoscales are still required in state-of-the-art ocean models. In this section we analyze how the Gent McWilliams
(GM) parameterization of eddy stirring (Gent and McWilliams, 1990; Gent et al., 1995) and the Redi isoneutral
245 diffusion (Redi, 1982) of tracers as implemented in FESOM2.0 impact the simulated ocean state.

246 The implementation of GM in FESOM2.0 (see Danilov et al., 2017 for more detail) follows the algorithm proposed by
247 Ferrari et al. (2010). It operates with explicitly defined eddy-induced velocity, which is different from that employed in
248 FESOM1.4, whereby skewness formulation as suggested by Griffies et al. (1998) is used. The scheme employed in
249 FESOM2.0 allows for natural tapering through the vertical elliptic operator and does not require an extra diagnostic of
250 eddy induced velocities which are, in contrast to FESOM1.4, explicitly defined. All specifications applicable to the GM
251 parameterization in FESOM1.4 have been ported to version 2.0. In the default model configuration the thickness
252 diffusivity coefficient is scaled vertically (see Ferreira et al., 2005; Wang et al., 2014) and also varies with horizontal
253 resolution. The maximum thickness diffusivity is set to 2000 m²/s and is gradually switched off starting from a
254 resolution of 40 km onwards. The Redi isoneutral diffusion is set equal to the thickness diffusivity following the tuning
255 experience gained with FESOM1.4. In order to verify the related model code and understand the effects of the GM and
256 isoneutral diffusion parameterizations newly implemented in FESOM2.0, we conducted four experiments where we
257 sequentially switch these parameterisations on and off.

260 3.2.1 Changes in hydrography

261 In the reference simulation we applied both the GM and Redi diffusion parameterizations. Then three sensitivity
262 simulations were carried out: In the first one we set the Redi diffusivity to zero, in the second we zeroed the GM stirring
263 coefficient, and in the third one we switched off both parameterizations. The simulated temperature and salinity biases
264 for the reference run and the differences between sensitivity and the reference simulations are shown in Fig. 6 and Fig.
265 7. Without Redi diffusivity, the modification of T and S within same density classes can only be realised via the vertical
266 turbulent closure or through the spurious mixing of the advection scheme (there is no explicit horizontal diffusion in
FESOM2.0). In this case there is no consistent way for the model to mix the water properties along isopycnals. Hence it



268 is not surprising that the absence of Redi results in the overall fresher upper ocean in response to reduced mixing of salt
between the deep and upper oceans. In patterns of horizontal anomaly it is especially seen in the Subpolar North
270 Atlantic (SNA) and in the vicinity of the convection zones. In the Southern Ocean (SO) the change in position of the
isopycnal slope is visualised in Fig. 10 via the meridional salinity section across 30°W as practiced in previous climate
272 studies (see eg. Armour et al., 2016). Although the slope of the Antarctic Intermediate Water (AAIW) in the SO is
predominantly determined by the interplay between Ekman pumping and eddy transport, isoneutral diffusion shows
274 pronounced impacts on the representation of water mass distribution. Without Redi the subsurface AAIW becomes
more saline while excessive freshwater accumulates within the upper 500 m. The increased presence of the freshwater
276 in the upper ocean strengthens the halocline and prevents the deep water production. Indeed, the corresponding
reduction of mixed layer depth (MLD) is shown in Fig. 8. Opposite to the upper ocean, except in the SNA, the deep
278 ocean shows the overall increase in salinity simply as a consequence of the total salt conservation in these experiments
(Fig. 7). As one might expect, the corresponding temperature change in the deep ocean in terms of buoyancy is opposite
280 to that in salinity.

282 In the experiment without GM parameterization, the isopycnal slope induced by the winds along the main oceanic
fronts reaches the critical value until it becomes unphysically balanced by processes like diffusion and numerical
284 mixing. In the absence of eddy counteraction effect, the Decon Cell circulation in the SO is strengthened in this
experiment, with stronger downwelling on the northern side of the Antarctic Circumpolar Current (ACC) and stronger
286 upwelling on the southern side (see section 3.2.2). As a consequence, the temperature and salinity shows negative and
positive anomalies on the northern and southern sides of the ACC, respectively. Although sharper isopycnal slopes are
288 expected to support deep convection, the MLD in this experiment did not change much as compared to the reference
configuration (see Fig. 8). Indeed, in contrast to the no-Redi experiment, the simulated slope of the AAIW isohalines in
290 the SO becomes unrealistically steep. As a result the surface freshwater penetrates along steep isopycnals to a deeper
depth than in the reference experiment. We conclude that a delicate interplay between GM and Redi parameterizations
292 is required in order to properly simulate the hydrographic properties in the global ocean using non eddy revolving
numerical grids.

294

3.2.2 Changes in thermohaline circulation

296 The influence of GM and Redi parameterizations on the thermohaline circulation is illustrated by the MOC (Fig. 9). In
runs without GM it is computed using only Eulerian velocities. In runs using GM, MOC contains both the Eulerian and
298 eddy-induced circulations. The latter ones are also shown separately in Suppl. 1. For the reference run the MOC
streamfunction is plotted in the upper panel of Fig. 9 and depicts the generally acceptable overturning circulation
300 patterns as is known from literature. The upper cell originates primarily from the Atlantic Ocean with the maximum
located at ~1000m depth. The maximum value is ~15 Sv at 40°N. The bottom cell for the AABW is contributed from
302 both Atlantic and Pacific oceans and is also well reproduced with the maximum strength of ~5 Sv.

The run with Redi diffusivity set to zero and GM on is distinguished by the smallest AMOC among those in the
304 sensitivity experiments. This agrees with the findings by Marshall et al., 2017. In contrast, the run without GM is
characterised by the largest AMOC. This is also an expected behaviour since without GM the isopycnal slopes become



306 steeper and induce stronger boundary currents accompanied by stronger return flows at depths. Align with findings by
307 Marshall et al. (2017), the bottom cell in the Atlantic Ocean, which indicates the spread of the AABW, is larger in runs
308 with GM. Interestingly, the bottom MOC cell for the global ocean is increased in all sensitivity experiments compared
309 to the reference run. As shown by Fig. 9 this is primarily due to the contribution from the Pacific Ocean. Furthermore it
310 shows an extremum at $\sim 40^\circ\text{N}$ which is absent in the reference simulation.

Our findings stress the importance of proper tuning of subgrid-scale parameterisations. The individual roles of Redi and
311 GM have been presented. Although their implementation in FESOM 2.0 is scale dependent a particular application
312 might require an additional tuning. Further sensitivity studies are required to better tune the value of eddy diffusivities
313 in these parameterizations.
314

3.3 Diapycnal Mixing

316 Mixing across density surfaces is an essential part of the thermohaline circulation. It can control not only the circulation
317 and heat budget of the global ocean, but also the distribution of nutrients and biological agents in the ocean (Wunsch
318 and Ferrari, 2004; De Lavergne et al., 2016). Therefore, a proper representation of diapycnal mixing in ocean models is
319 essential. Mixing processes are not resolved in ocean models except in very limited domains and have to be
320 parameterized. Current climate models are often utilized with the Pacanowski and Philander (1981, hereafter as PP) or
321 the K-Profile Parameterization (KPP, Large et al., 1994) vertical mixing schemes, depending on the physical
322 complexity they address. Both mixing schemes are implemented in FESOM2.0 in a slightly modified version. During
323 the tuning and parameter testing phase, and based on our experience with FESOM1.4, it is found necessary to slightly
324 modify both mixing schemes compared to the original implementation of Pacanowski and Philander (1981) and Large
325 et al., (1994), with respect to the used background vertical diffusivity and additional vertical mixing depending on the
326 diagnostically computed Monin–Obukhov length, to overcome certain biases especially in the Arctic region and
327 Southern Ocean.

328
The Pacanowski and Philander (PP) scheme used in FESOM2.0 computes the subgrid-scale turbulent vertical kinematic
329 flux of tracer and momentum via the local Richardson number (Ri). The vertical background viscosity for momentum is
330 set to $1 \cdot 10^{-4} \text{ m}^2/\text{s}$. For potential temperature and salinity we deviate from the standard PP implementation and use a
331 non constant, depth and latitude dependent background diffusivity with values between $1 \cdot 10^{-4} \text{ m}^2/\text{s}$ and $1 \cdot 10^{-6} \text{ m}^2/\text{s}$
332 (see Suppl. 3). The original PP scheme, as well as the PP scheme used in FESOM1.4 used here a constant background
333 diffusivity. For the convection case ($Ri < 0$), vertical diffusivity and viscosity is set to $0.1 \text{ m}^2/\text{s}$ in order to remove static
334 instability to ensure stable density profiles.

336 The original PP scheme is further augmented by the mixing scheme proposed by Timmermann et al. (2003). In this
337 scheme, the vertical mixing within the diagnostically computed Monin–Obukhov length, which depends on surface
338 friction velocity, the sea ice drift velocity and surface buoyancy flux, is increased to a value of $0.01 \text{ m}^2/\text{s}$ to further stir
339 the seasonal varying wind-mixed layer depth. This strongly reduced the hydrography biases, especially in the Southern
340 Ocean (not shown).

342 In contrast to the PP scheme, the KPP scheme explicitly calculates diffusivity throughout the boundary layer and
provides a smooth transition to the interior diffusivity. Within the boundary layer, scalar fields (temperature and



344 salinity) obtain a countergradient transport term provided that the net surface buoyancy forcing flux is unstable. In the
345 current version of FESOM2.0, the background diffusivity in KPP uses the same non-constant latitude and depth
346 dependent background diffusivities as in PP. Maximum diffusivity and viscosity due to shear instability are set to be
347 $5.0 \cdot 10^{-2}$ and $5.0 \cdot 10^{-3}$, respectively. The magnitude of the tracer diffusivities is reduced one order of magnitude
348 between the equatorial belt of 5° S and 5° N following the observations of Gregg et al. (2003). Also the KPP scheme is
augmented by the same mixing scheme proposed by Timmermann et al. (2003) and that is used in PP.

350

In order to show the sensitivity to the choice of the vertical mixing schemes, two simulations with different vertical
352 mixing schemes are conducted. The depth-integrated model biases of the surface, mid-ocean and deep-ocean are shown
for temperature and salinity in Fig. 11 and Fig. 12, respectively. Compared to WOA05, the KPP simulation generally
354 overestimates ocean temperatures in the surface layers in the Kuroshio region, equatorial belt, Indian Ocean and
Southern Ocean, and underestimates them in the subtropics and North Atlantic subpolar gyre region. In the mid- and
356 deep ocean, temperature is generally overestimated, except for the ACC and the North Atlantic.

Differences in the open ocean between PP and KPP experiments are very small, compared to the model bias with
358 respect to WOA05. The largest differences between these experiments in the surface layers exist in the equatorial
Pacific, where temperature simulated with PP is colder than in the case of KPP. In the deep ocean, temperature is
360 generally warmer in PP than in the KPP experiment. The relatively small differences between the two experiments
might be related to the fact that the same background diffusivity and the same Monin-Obukhov length scale are applied.
362 The salinity bias in different depth ranges is shown in Fig. 12. Notably, KPP and PP simulate similar departures from
WOA05, particularly large in the surface waters of the Arctic Ocean and North Atlantic. Both experiments show much
364 lower salinities than the climatology. The deep-ocean salinity bias might be caused by the wrong characteristics of
Mediterranean plume entering into the Atlantic Ocean. Using the PP scheme in simulations has less salinity biases in
366 the surface layers in the subpolar gyre region. Besides, in the mid-depth, KPP simulated a saltier tropical Atlantic
compared to PP.

368 The KPP and PP vertical mixing schemes, in their current implementation, reproduce a very similar ocean state, where
PP is slightly better in modelling the upper ocean until 500m while KPP is slightly better in modelling the deeper ocean
370 >500 m. In coupled climate model simulations, the KPP scheme was found to cause stronger open-ocean convection that
leads to a stronger and stable AMOC compared to the PP scheme (Gutjahr et al., 2018). Our ocean-alone simulations
372 show similar tendency in terms of MLD in the NA subpolar gyre, but have relatively small difference in the AMOC
strength (see Suppl. 2). This implies that the interaction between the ocean and active atmosphere might exaggerate the
374 effect of different mixing schemes. The assessment of vertical mixing schemes in FESOM2.0 coupled model
simulations will be carried out in the course of our coupled model development.

376 **4 Comparison between FESOM1.4 and FESOM2.0**

4.1 Differences in hydrography and thermohaline circulation

378 The purpose of this section is to show that FESOM2.0 has evolved to a point where it is able to reproduce a realistic
ocean state that is comparable to its predecessor FESOM1.4. For this purpose we run both model versions in the linfs
380 configuration using the coarse reference mesh and CORE-II atmospheric forcing. This configuration is used here



because it was employed for the systematic assessment of FESOM1.4 in the CORE-II model intercomparison project.
382 Although we use the same 2D mesh and vertical discretization in both models, it should be kept in mind that
FESOM2.0 uses prismatic elements while FESOM1.4 uses tetrahedral elements, and the numerical cores and the
384 implementation of eddy parameterizations are different.

386 Fig. 14 shows the biases of the modeled ocean temperature with FESOM2.0 and FESOM1.4 in three different depth
ranges averaged for the period 1998-2007 and referenced to the WOA05 climatology. FESOM2.0 shows for the surface
388 depth range a stronger warm bias in the area of the East and West Greenland current and Labrador current, together
with a reduced North Atlantic cold bias. The cold bias in the eastern Pacific is particularly stronger than in FESOM1.4.
390 In addition, the surface depth range in FESOM2.0 features a slightly warmer equatorial ocean, North Pacific and Indian
Ocean than FESOM1.4, while the situation in the Southern Ocean is reversed. The intermediate depth range simulated
392 with FESOM2.0 shows in general higher warm biases in the northern and southern Pacific, Indian Ocean and in the
region of the Kuroshio Current, while the intermediate depth range simulated with FESOM1.4 is dominated by a cool
394 bias for the tropical and subtropical Pacific and North Atlantic. The depth range of 500-1000 m reveals for FESOM2.0 a
general warming bias except for the Southern Ocean and the North Atlantic. The deep depth range of FESOM1.4
396 is dominated by a particularly stronger cold bias for the North Atlantic and Indian Ocean, while the biases in the Pacific
and Arctic Ocean seem to be lower.

398 The salinity biases in the simulations are shown in Fig. 15. Both models indicate a freshening bias for the Arctic Ocean
through all considered depth ranges, where the fresh bias in FESOM2.0 seems to be slightly stronger. Both models
400 reveal quite similar bias patterns for the rest of the global ocean, where the saline biases are more pronounced in
FESOM2.0, while the fresh biases are stronger in FESOM1.4.

402 The northern hemispheric March and southern hemispheric September mean MLD (Monterey and Levitus, 1997)
shown in Fig. 16 simulated with FESOM2.0 and FESOM1.4 reveal that FESOM2.0 tends to produce higher and
404 spatially more extended March MLD values in the Labrador Sea and Irminger Sea but also in the GIN Sea. On the
southern hemisphere the difference is even more pronounced, here only FESOM2.0 produces significant MLD values in
406 the Weddell Sea, while FESOM1.4 reveals almost no MLD activity.

The streamfunctions of the meridional overturning circulation simulated with FESOM2.0 and FESOM1.4 are shown in
408 Fig. 17, globally (upper row), for the Atlantic (middle row) and for the Indo-Pacific region (lower row). It is shown that
globally FESOM2.0 tends to produce less AABW with a strength of up to ~5 Sv, compared to FESOM1.4 with a
410 strength of up to 10 Sv, which is at the upper boundary of acceptable values shown by other ocean models (Griffies et
al., 2009; Danabasoglu et al., 2019). The FESOM2.0 simulation indicates a stronger northward extend of the AABW
412 cell until ~60°N. The upper AMOC cell, which represents the formation of NADW is clearly stronger in the FESOM2.0
model simulation, with a strength of 15 Sv compared to 10 Sv in FESOM1.4.

414 The salinity sections at -30°W from -80°S to 40°N averaged for the period 1998-2007 (Fig. 18) show that both models
are good at reproducing the low salinity tongue of AAIW that spreads northward. In FESOM2.0 the AAIW reaches
416 slightly less far north than in FESOM1.4, which also does not reach the northward extend of AAIW that the WOA05
data let suggest. FESOM2.0 reveals a weaker surface stratification south of -60°S than FESOM1.4. The salinity values
418 below 1000m depth and south of -50°S in the FESOM2.0 simulation are lower than in FESOM1.4, implying stronger
influence from the fresh Antarctic Shelf Water.



420 4.2 Scaling and Performance

Both considered model versions, FESOM2.0 and FESOM1.4 are written in Fortran 90 with some C/C++ snippets for
422 the binding of third party libraries. The code of both model versions uses a distributed memory parallelization based on
the Message Passing Interface MPI. One of the main differences between FESOM2.0 and FESOM1.4, besides their
424 finite-volume and finite-element numerical cores, is the treatment of 3D variables. FESOM1.4 works with 3D
tetrahedral elements, so their vertices are not defined by surface vertices, which requires full 3D lookup tables to
426 address the fields on tetrahedra and 3D auxiliary arrays for computations of derivatives. FESOM2.0, on the other hand,
performs computations in 3D on prismatic elements, which preserve their horizontal connectivity over depth. In this
428 case 2D lookup tables can be used, which boosts the performance of the model. All simulations shown here were
carried out on a Cray CS400 system with 308 compute nodes, where each compute node is equipped with 2x Intel Xeon
430 Broadwell 18-Core CPUs with 64GB RAM (DDR4 2400MHz) provided by the Alfred Wegener Institute Helmholtz
Centre for Polar and Marine Research. The performance of both model versions on this machine running for 1000
432 simulated time steps were tested for a different number of cores and shown in Fig. 19.

For the scalability tests a medium-sized mesh configurations was chosen (see Fig. 1 right), which was already used in
434 previous publications, with 638387 surface vertices and a minimal resolution of 4.5 km in the Arctic (Wang et al.,
2018). The performance results were obtained by using the nonlinear free surface mode, GM and Redi parameterisation
436 and the KPP vertical mixing and taking into account only the time the models require to solve the ocean and sea ice
components, disregarding input/output and the initialization phase (setting up arrays, reading the mesh etc.). Both model
438 versions show a parallel total scalability until at least 2304 cores, beyond that FESOM2.0 starts to saturate, while
FESOM1.4 still reveals linear scalability at least until 4608 cores. The reduction in scalability of FESOM2.0 is partly
440 caused by the sea ice component due to an extensive communication in the elastic-viscous-plastic sea ice solver of
FESIM (Danilov et al., 2015). The other source of lacking scalability is the solver for the external mode in the ocean
442 component. We use pARMS- parallel Algebraic Recursive Multilevel Solver (Li et al., 2003) to iteratively solve for the
elevation, which loses scalability towards large number of cores (not shown). This issue will be addressed in a separate
444 publication. Since the 3D part of FESOM2.0 is much faster than that of FESOM1.4, the scalability of FESOM2.0 shows
earlier saturation, which is limited by 2D parts in both codes.

446 Using the low resolution reference mesh (127000 surface vertices, Fig. 1 left), on 432 cores of the aforementioned
machine, neglecting the time for input and output, using a time step of 45 minutes, FESOM1.4 reaches a throughput of
448 62 simulated years per day (SYPD), spending 91.9% and 8.1% in the ocean- and ice step, respectively. Running the
model on the same mesh, with the same computer resources and time step with FESOM2.0, a throughput of 191 SYPD
450 is reached, with the model spending 74.7% and 25.3% of its runtime in the ocean- and ice step, respectively. In the
ocean step, 16.4% and 23.4% of the time is used for the dynamical calculation of u, v, w and ssh, respectively, 39.4%
452 of the ocean step runtime is used to solve the equations for the temperature and salinity. The implementation of GM
following Ferrari et al. (2010) and Redi diffusion accounts for 3.9% of the ocean step runtime. With the medium-sized
454 mesh configuration (638387 surface vertices, Fig. 1 right) used for the scalability tests, running on 2304 cores with a
time steps of 15 minutes, FESOM1.4 and FESOM2.0 reach a throughput of 20 SYPD and 59 SYPD, respectively.

456 The numbers given in this section should only serve as a guideline for the performance of FESOM2.0, the details can
vary depending on the machine that is used, the frequency of writing the output, the type of advection schemes, the type
458 of mixing schemes and the number of subcycles used in the elastic-viscous-plastic sea ice solver. Nevertheless, a



460 realistic performance estimate for FESOM2.0 is a speedup by a factor of 2.8 to 3.4 compared to FESOM1.4, depending
461 on the aforementioned factors.

4.3 Meshes used

462 In the recent years, as FESOM1.4 had matured from its early days, a plenty of FESOM-based studies have been carried
463 out, covering a wide range of application and scientific questions, using a large number of very different mesh
464 configurations. Fig. 20 gives a schematic of only a small collection of surface unstructured meshes from studies already
465 published or in progress.

466 The range of available meshes shown in Fig. 20 starts at rather small mesh sizes with less than 250K surface vertices.
467 For comparison we mention that a conventional 0.25 (0.5) degree quadrilateral mesh contains about 1M (250K) of wet
468 vertices. These small meshes are used especially for testing and tuning purposes but also for long fully coupled present-
469 day and scenario climate studies (Sidorenko et al. 2014, 2018; Rackow et al. 2018; Wang et al., 2014; Sein et al., 2018;
470 Wang et al., 2019a) and paleo applications (Shi et al., 2016) with AWI-CM. Using the coarse reference mesh
471 configuration (~127K surface vertices, also shown in Fig. 1 left) it has been shown that FESOM1.4 performs as well as
472 a variety of coarse structured mesh ocean models, in terms of modeled general ocean circulation (e.g Danabasoglu
473 et al., 2016; Wang et al., 2016a, 2016b). The range of medium-sized meshes between 500K until 2000K surface vertices,
474 includes the meshes with either globally increased resolution to a higher extent or locally strongly refined key regions
475 of interest (Wang et al., 2016, 2018a,b, 2019b; Wekerle et al. 2017; Sein et al. 2016, 2018). Using FESOM1.4 it was
476 shown that this class of meshes are well suited for ocean only simulations, as well as for fully coupled model
477 simulations, which, however, require sufficiently large amounts of computational resources. Using FESOM1.4 Wekerle
478 et al. (2017) and Wang et al. (2018a) have shown that by homogeneously increasing the resolution in the Arctic Ocean
479 to 4.5 km (the mesh with ~640K surface vertices in Fig. 20 and Fig. 1 right) the representation of Atlantic water in the
480 Nordic Sea and the Arctic Basin can be significantly improved by only moderately increasing the computational costs.
481 In Sein et al. (2016), FESOM1.4 was used to show that a mesh configuration with increased resolution in dynamically
482 active regions (the mesh with ~1.31M surface vertices in Fig. 20, minimum resolution 10km), determined by observed
483 high sea surface height variability, can significantly improve simulated ocean variability and hydrography with respect
484 to observations.

485 In order to appropriately simulate mesoscale eddies, the Rossby deformation radius needs to be resolved with several
486 grid points (Hallberg, 2013). Sein et al. (2017) introduced a mesh, where the Rossby radius is resolved by two grid cells
487 with the minimum resolution set to 4 km on the northern hemisphere and 7 km on the southern hemisphere (the mesh
488 with ~5.01M surface vertices Fig. 20). Another mesh of similar size with a global homogeneous resolution of 1/10°
489 adapted from the MPIOM STROM configuration (von Storch et al., 2012) (~5.58M surface vertices in Fig. 20) by
490 splitting quads into triangles was also tested. While FESOM1.4 can still be used in these cases, it requires >7000 cores
491 to reach a throughput of 1.5 SYPD. It became obvious that at around 5M to 6M surface nodes FESOM1.4 reaches its
492 practical limit in terms of routinely available computational resources. However, the increased computational
493 performance of FESOM2.0 with three times the throughput of FESOM1.4 allows to use larger meshes to address new
494 research questions. Fig. 20 shows two upcoming very large meshes (>6M surface vertices) created for FESOM2.0 that
495 were already used in test simulations. One of them focuses on the Arctic Ocean. Since the Rossby deformation radius is
496 latitude dependent, it becomes very small in polar regions, which makes mesoscale resolving simulations for those



regions a highly challenging task. This configuration consists of ~11.83M surface vertices, featuring a background
498 resolution of $\sim 1^\circ$, a latitudinal increasing resolution for the entire Atlantic varying from 0.5° to $1/15^\circ$ between -20°S and
75°N, and a mesoscale and partially sub-mesoscale eddy resolving resolution of 1 km for the entire Arctic Ocean. The
500 other mesh configuration consists of ~16.18M surface vertices and resolves the Rossby deformation radius with four
grid cells on a global scale with a cutoff resolution of 2 km and 4 km for the northern and southern hemisphere,
502 respectively.

The upcoming version of AWI-CM using FESOM2.0 will allow us to also expand the mesh applicability for long
504 climate simulations from small-sized towards medium and large-sized mesh configurations.

506 5 Discussion and Conclusions

Currently FESOM 2.0 possesses all the features available in FESOM 1.4 and offers more flexibility which results
508 mainly from the ALE implementation of the vertical coordinate in the new model version. Although many features are
common between the two versions, applying the same surface forcing and initial conditions leads to certain difference
510 in modelled ocean states. Part of these difference result from the slightly different implementation of parameterisation
schemes and consequently the different set of tuning parameters. This includes the implementation of GM after Ferrari
512 et al. 2010 (i.e. solving a boundary-value problem on eddy-induced transport streamfunction) in FESOM 2.0 and after
Griffies et al. (1998) (i.e. using the skew flux formulation for eddy-induced transport) in FESOM 1.4. Part of the
514 differences can also originate from the implicit numerical mixing associated with different numerics in the two versions
of the model. The analysis of the numerical mixing in FESOM 2.0 associated with advection schemes will be described
516 in another paper.

The presented comparison between FESOM1.4 and FESOM2.0 in terms of hydrography proved that FESOM2.0 is at a
518 stage where it is ready to replace FESOM1.4. Both model versions show a similar magnitude of the biases in
temperature and salinity. There are spatial differences, however, especially in the Pacific and Indian Ocean, which can
520 be attributed to general differences in the numerical core as well as different implementation of schemes like the GM
parameterisation. The meridional overturning between FESOM1.4 and FESOM2.0 reveals some obvious differences,
522 especially in the case of the AMOC. Here FESOM2.0 simulates a significantly stronger upper AMOC cell, with a
strength of ~ 15 Sv, while FESOM1.4 is known to simulate a weaker upper AMOC cell (Sidorenko et al., 2011), with a
524 strength of ~ 10 Sv, which is at the lower range of acceptable values simulated by other ocean models (Griffith et al.,
2009). Observational AMOC estimates suggest an AMOC strength of ~ 17.5 Sv at 26°N (Smeed et al., 2014; McCarthy
526 et al., 2015), which is much closer to the simulated value of FESOM2.0.

It is worth mentioning that the analysis of transports is significantly simplified in FESOM 2.0 as compared to that in
528 FESOM1.4. In the continuous finite element discretisation of FESOM1.4 the interpretation of fluxes is ambiguous since
the model equations are discretized in a weak sense through weighting with some test functions. This makes it difficult
530 to perform the analysis of overturning circulation streamfunctions or even the volume fluxes from the computed
velocities without the usage of additional techniques for the proper flux interpretation (see eg. Sidorenko et al., 2009).
532 In FESOM 2.0 the model fluxes are explicitly defined and their interpretation is straightforward.

FESOM1.4 had a throughput that is around three times lower compared to regular grid models of similar complexity.
534 With the three fold increase in computational performance of FESOM2.0, we are now able to offer for the first time an



536 unstructured-mesh model that is able to run as fast as or even faster than regular-mesh models. For example, Prims et al.
537 (2018) show that the state-of-the-art NEMO model in a $\frac{1}{4}$ degree configuration is able to obtain around 3 SYPD using
538 512 cores; however, scalability is already lost when going to a higher number of cores. Using the same number of cores
539 on the aforementioned machine, with a mesh that has a resolution of $\frac{1}{4}$ degree (the mesh with $\sim 910K$ surface vertices
540 in Fig. 20), FESOM2.0 reaches a throughput of more than 5 SYPD.

541 FESOM2.0 can reach such a high throughput because the unstructuredness of its meshes is confined to the horizontal
542 direction, while the vertical direction is structured and prismatic elements are used. In this case, look-up tables and the
543 corresponding auxiliary arrays are only two dimensional and need to be accessed just once and can then be used over
544 the entire water column, which makes the cost of accessing them rather low compared to FESOM1.4. We suspect that
545 unstructured-mesh models also benefit from the fact that only wet nodes are accessed, which could partly explain why
546 FESOM2.0 outperforms some models using structured meshes.

547 Development of FESOM2 will continue during the next few years. The external vertical mixing library CVMIX will be
548 added into FESOM2.0 and tested, including the new energy consistent vertical mixing parameterization IDEMIX
549 (Olbers et al., 2017; Eden et al., 2017; Pollman et al., 2017). The development of the new coupled system AWI-CM
550 using FESOM2.0 is finished in support for a variety of climate scale applications with time frames from paleo to future
551 scenarios as required by the climate research community. The final tuning for the new AWI-CM is underway. The
552 development team also works on new higher order advection schemes for tracer and momentum. Although for the
553 moment only the usage of the linear free surface and full free surface option are implemented in the code with the ALE
554 approach, the implementation of terrain-following and hybrid coordinates will follow.

555 Despite of the existing remarkable computational performance of FESOM2.0, there is still potential for future
556 improvements by tackling performance bottlenecks, such as, by calling the sea ice step just every second or other ocean
557 step, which could help to delay scalability saturation in the sea ice component due to the EVP subcycling, as well as to
558 explore the use of subcycling for the sea surface height solver. However, these potential performance improvements
559 will be explored in an own publication. Further improvements can be the use of hybrid meshes composed of triangles
560 and quads (Danilov et al., 2014), which could reduce the number of edge cycles and further speed up the code
561 performance.

562 This paper is the first in a series of papers to document the development and assessment of important key components
563 of FESOM2.0 in realistic global model configurations. We described the implementation and associated simulation
564 biases of some simple ALE options, that is, the linear free and full free surface formulations. Furthermore, we discussed
565 the effect of GM parameterization, isoneutral Redi diffusion and KPP versus PP vertical mixing schemes. In particular,
566 the relative role of the GM and Redi diffusion parameterizations are assessed. The manuscript also shows that the
567 results of FESOM2.0 compare well to FESOM1.4 in terms of model biases and ocean circulation, but with a remarkable
568 performance speedup by a factor of three mainly due to its superior data structure. In addition, FESOM2.0 shows a
569 more realistic AMOC strength, combined with a convenient computation of transports.
570



572 **Author contributions**

Dmitry Sidorenko, Sergey Danilov, Patrick Scholz, Ozgur Gurses, Margarita Smolentseva as well as Natalja Rakowsky
574 worked on the development of the FESOM2.0 model code. The tuning of the model as well as all simulation shown in
this paper were carried out by Patrick Scholz, Dmitry Sidorenko and Ozgur Gurses, which were also responsible for
576 preparing the basic manuscript. Qiang Wang, Sergey Danilov, Nikolay Koldunov, Dmitry Sein and Thomas Jung have
contributed to the final version of the manuscript.

578 **Acknowledgements**

This paper is a contribution to the project S2: Improved parameterisations and numerics in climate models and S1:
580 Diagnosis and Metrics in Climate Models of the Collaborative Research Centre TRR 181 "Energy Transfer in
Atmosphere and Ocean" funded by the Deutsche Forschungsgemeinschaft (DFG, German Research Foundation) -
582 Projektnummer 274762653.

584 **Code availability**

The FESOM2.0 version used to carried out the simulations reported here is available from
586 <https://gitlab.dkrz.de/FESOM/fesom2/tags/2.0.2> after registration, for convenience (without registration) the FESOM2.0
code is also available under <https://doi.org/10.5281/zenodo.2348928>. FESOM1.4 can be downloaded from
588 <https://swrepo1.awi.de/projects/fesom> after registration. For the sake of the journal requirement, the code can be also
achieved at <https://doi.org/10.5281/zenodo.1116851>. The used mesh, as well as the temperature, salinity and vertical
590 velocity (for the calculation of the MOC) data of all conducted simulations can be found under
https://swiftbrowser.dkrz.de/public/dkrz_035d8f6ff058403bb42f8302e6badfbc/
592 [FESOM2.0_evaluation_part1_scholz_etal/](#). The simulation results can be also obtained from the authors on request.
Mesh partitioning in FESOM2.0 is based on a METIS version 5.1.0 package developed at the Department of Computer
594 Science and Engineering at the University of Minnesota (<http://glaros.dtc.umn.edu/gkhome/views/metis>). METIS and
the solver pARMS (Li et al., 2003) present separate libraries which are freely available subject to their licenses. The
596 Polar Science Center Hydrographic Climatology (Steele et al., 2001) used for model initialization and the CORE-II
atmospheric forcing data (Large and Yeager, 2009) are freely available online.

598

References

- 600 Antonov, J. I., R. A. Locarnini, T. P. Boyer, A. V. Mishonov, and H. E. Garcia, World Ocean Atlas 2005, Volume 2:
Salinity. S. Levitus, Ed. NOAA Atlas NESDIS 62, U.S. Government Printing Office, Washington, D.C., 182
602 pp., 2006
- Biastoch, A., Sein, D., Durgadoo, J. V., Wang, Q. and Danilov, S.: Simulating the Agulhas system in global ocean
604 models – nesting vs. multi-resolution unstructured meshes, *Ocean Modelling*, 121, 117–131,
doi:10.1016/j.ocemod.2017.12.002, 2018.



- 606 Carter, L., Mccave, I. and Williams, M. J.: Chapter 4 Circulation and Water Masses of the Southern Ocean: A Review,
Antarctic Climate Evolution Developments in Earth and Environmental Sciences, 85–114, doi:10.1016/s1571-
608 9197(08)00004-9, 2008.
- 610 Danabasoglu, G., Yeager, S. G., Bailey, D., Behrens, E., Bentsen, M., Bi, D., Biastoch, A., Böning, C., Bozec, A.,
Canuto, V. M., Cassou, C., Chassignet, E., Coward, A. C., Danilov, S., Diansky, N., Drange, H., Farneti, R.,
612 Fernandez, E., Fogli, P. G., Forget, G., Fujii, Y., Griffies, S. M., Gusev, A., Heimbach, P., Howard, A., Jung, T.,
Kelley, M., Large, W. G., Leboissetier, A., Lu, J., Madec, G., Marsland, S. J., Masina, S., Navarra, A., Nurser,
A. G., Pirani, A., Mélia, D. S. Y., Samuels, B. L., Scheinert, M., Sidorenko, D., Treguier, A.-M., Tsujino, H.,
614 Uotila, P., Valcke, S., Voldoire, A. and Wang, Q.: North Atlantic simulations in Coordinated Ocean-ice
Reference Experiments phase II (CORE-II). Part I: Mean states, *Ocean Modelling*, 73, 76–107,
616 doi:10.1016/j.ocemod.2013.10.005, 2014.
- 618 Danabasoglu, G., Yeager, S. G., Kim, W. M., Behrens, E., Bentsen, M., Bi, D., Biastoch, A., Bleck, R., Böning, C.,
Bozec, A., Canuto, V. M., Cassou, C., Chassignet, E., Coward, A. C., Danilov, S., Diansky, N., Drange, H.,
Farneti, R., Fernandez, E., Fogli, P. G., Forget, G., Fujii, Y., Griffies, S. M., Gusev, A., Heimbach, P., Howard,
620 A., Ilicak, M., Jung, T., Karspeck, A. R., Kelley, M., Large, W. G., Leboissetier, A., Lu, J., Madec, G.,
Marsland, S. J., Masina, S., Navarra, A., Nurser, A. G., Pirani, A., Romanou, A., Mélia, D. S. Y., Samuels, B. L.,
622 Scheinert, M., Sidorenko, D., Sun, S., Treguier, A.-M., Tsujino, H., Uotila, P., Valcke, S., Voldoire, A., Wang,
Q. and Yashayaev, I.: North Atlantic simulations in Coordinated Ocean-ice Reference Experiments phase II
624 (CORE-II). Part II: Inter-annual to decadal variability, *Ocean Modelling*, 97, 65–90,
doi:10.1016/j.ocemod.2015.11.007, 2016.
- 626 Danilov, S. and Androsov, A.: Cell-vertex discretization of shallow water equations on mixed unstructured meshes,
Ocean Dynamics, 65(1), 33–47, doi:10.1007/s10236-014-0790-x, 2014.
- 628 Danilov, S., Wang, Q., Timmermann, R., Iakovlev, N., Sidorenko, D., Kimmritz, M., Jung, T. and Schröter, J.: Finite-
Element Sea Ice Model (FESIM), version 2, *Geoscientific Model Development Discussions*, 8(2), 855–896,
630 doi:10.5194/gmdd-8-855-2015, 2015.
- Danilov, S., Sidorenko, D., Wang, Q. and Jung, T.: The Finite-volumE Sea ice–Ocean Model (FESOM2), *Geoscientific
632 Model Development*, 10(2), 765–789, doi:10.5194/gmd-10-765-2017, 2017.
- Danilov, S., Kivman, G. and Schröter, J.: A finite-element ocean model: principles and evaluation, *Ocean Modelling*,
634 6(2), 125–150, doi:10.1016/s1463-5003(02)00063-x, 2004.
- Donea, J. and Huerta, A.: *Finite element methods for flow problems*, Wiley., 2005.
- 636 Eden, C. and Olbers, D.: A Closure for Internal Wave–Mean Flow Interaction. Part II: Wave Drag, *Journal of Physical
Oceanography*, 47(6), 1403–1412, doi:10.1175/jpo-d-16-0056.1, 2017.
- 638 Ferrari, R., Griffies, S. M., Nurser, A. G. and Vallis, G. K.: A boundary-value problem for the parameterized mesoscale
eddy transport, *Ocean Modelling*, 32(3-4), 143–156, doi:10.1016/j.ocemod.2010.01.004, 2010.
- 640 Ferreira, D., Marshall, J. and Heimbach, P.: Estimating Eddy Stresses by Fitting Dynamics to Observations Using a
Residual-Mean Ocean Circulation Model and Its Adjoint, *Journal of Physical Oceanography*, 35(10), 1891–
642 1910, doi:10.1175/jpo2785.1, 2005.
- Gent, P. R. and McWilliams, J. C.: Isopycnal Mixing in Ocean Circulation Models, *Journal of Physical Oceanography*,
644 20(1), 150–155, doi:10.1175/1520-0485(1990)020<0150:imiocm>2.0.co;2, 1990.



- 646 Gent, P. R., Willebrand, J., Mcdougall, T. J. and McWilliams, J. C.: Parameterizing Eddy-Induced Tracer Transports in
Ocean Circulation Models, *Journal of Physical Oceanography*, 25(4), 463–474, doi:10.1175/1520-
0485(1995)025<0463:peitti>2.0.co;2, 1995.
- 648 Gregg, W. W., Conkright, M. E., Ginoux, P., O'reilly, J. E. and Casey, N. W.: Ocean primary production and climate:
Global decadal changes, *Geophysical Research Letters*, 30(15), doi:10.1029/2003gl016889, 2003.
- 650 Griffies, S. M., Biastoch, A., Böning, C., Bryan, F., Danabasoglu, G., Chassignet, E. P., England, M. H., Gerdes, R.,
Haak, H., Hallberg, R. W., Hazeleger, W., Jungclaus, J., Large, W. G., Madec, G., Pirani, A., Samuels, B. L.,
652 Scheinert, M., Gupta, A. S., Severijns, C. A., Simmons, H. L., Treguier, A. M., Winton, M., Yeager, S. and Yin,
J.: Coordinated Ocean-ice Reference Experiments (COREs), *Ocean Modelling*, 26(1-2), 1–46,
654 doi:10.1016/j.ocemod.2008.08.007, 2009.
- Griffies, S. M.: *Fundamentals of ocean climate models*, Princeton University Press., 2004.
- 656 Griffies, S. M.: The Gent–McWilliams Skew Flux, *Journal of Physical Oceanography*, 28(5), 831–841,
doi:10.1175/1520-0485(1998)028<0831:tgmsf>2.0.co;2, 1998.
- 658 Griffies, S. M., Yin, J., Durack, P. J., Goddard, P., Bates, S. C., Behrens, E., Bentsen, M., Bi, D., Biastoch, A., Böning,
C. W., Bozec, A., Chassignet, E., Danabasoglu, G., Danilov, S., Domingues, C. M., Drange, H., Farneti, R.,
660 Fernandez, E., Greatbatch, R. J., Holland, D. M., Ilicak, M., Large, W. G., Lorbacher, K., Lu, J., Marsland, S. J.,
Mishra, A., Nurser, A. G., Méliá, D. S. Y., Palter, J. B., Samuels, B. L., Schröter, J., Schwarzkopf, F. U.,
662 Sidorenko, D., Treguier, A. M., Tseng, Y.-H., Tsujino, H., Uotila, P., Valcke, S., Voldoire, A., Wang, Q.,
Winton, M. and Zhang, X.: An assessment of global and regional sea level for years 1993–2007 in a suite of
664 interannual CORE-II simulations, *Ocean Modelling*, 78, 35–89, doi:10.1016/j.ocemod.2014.03.004, 2014.
- Gutjahr, O., Putrasahan, D., Lohmann, K., Jungclaus, J. H., von Storch, J.-S., Brüggemann, N., Haak, H., and Stössel,
666 A.: Max Planck Institute Earth System Model (MPI-ESM1.2) for High-Resolution Model Intercomparison
Project (HighResMIP), *Geosci. Model Dev. Discuss.*, <https://doi.org/10.5194/gmd-2018-286>, in review, 2018.
- 668 Hallberg, R.: Using a resolution function to regulate parameterizations of oceanic mesoscale eddy effects, *Ocean
Modelling*, 72, 92–103, doi:10.1016/j.ocemod.2013.08.007, 2013.
- 670 Korn, P.: Formulation of an unstructured grid model for global ocean dynamics, *Journal of Computational Physics*, 339,
525–552, doi:10.1016/j.jcp.2017.03.009, 2017.
- 672 Kuhlbrodt, T., Griesel, A., Montoya, M., Levermann, A., Hofmann, M. and Rahmstorf, S.: On the driving processes of
the Atlantic meridional overturning circulation, *Reviews of Geophysics*, 45(2), doi:10.1029/2004rg000166,
674 2007.
- Large, W. G., McWilliams, J. C. and Doney, S. C.: Oceanic vertical mixing: A review and a model with a nonlocal
676 boundary layer parameterization, *Reviews of Geophysics*, 32(4), 363, doi:10.1029/94rg01872, 1994.
- Large, W. G. and Yeager, S. G.: The global climatology of an interannually varying air–sea flux data set, *Climate
678 Dynamics*, 33(2-3), 341–364, doi:10.1007/s00382-008-0441-3, 2008.
- Large, W. G., Danabasoglu, G., Doney, S. C. and McWilliams, J. C.: Sensitivity to Surface Forcing and Boundary Layer
680 Mixing in a Global Ocean Model: Annual-Mean Climatology, *Journal of Physical Oceanography*, 27(11), 2418–
2447, doi:10.1175/1520-0485(1997)027<2418:stsfab>2.0.co;2, 1997.
- 682 Lavergne, C. D., Madec, G., Sommer, J. L., Nurser, A. J. G. and Garabato, A. C. N.: On the Consumption of Antarctic
Bottom Water in the Abyssal Ocean, *Journal of Physical Oceanography*, 46(2), 635–661, doi:10.1175/jpo-d-14-



- 684 0201.1, 2016.
- Li, Z., Saad, Y. and Sosonkina, M.: pARMS: a parallel version of the algebraic recursive multilevel solver, *Numerical*
686 *Linear Algebra with Applications*, 10(5-6), 485–509, doi:10.1002/nla.325, 2003.
- Locarnini, R. A., A. V. Mishonov, J. I. Antonov, T. P. Boyer, and H. E. Garcia., *World Ocean Atlas 2005, Volume 1:*
688 *Temperature*. S. Levitus, Ed. NOAA Atlas NESDIS 61, U.S. Government Printing Office, Washington, D.C.,
182 pp. , 2006.
- 690 Marshall, J., Scott J. R., Romanou A., Kelley M., Leboissetier A., The dependence of the ocean’s MOC on mesoscale
eddy diffusivities: A model study, *Ocean Modelling*, Volume 111, Pages 1-8, ISSN 1463-5003,
692 <https://doi.org/10.1016/j.ocemod.2017.01.001>, 2017.
- Mccarthy, G., Smeed, D., Johns, W., Frajka-Williams, E., Moat, B., Rayner, D., Baringer, M., Meinen, C., Collins, J.
694 and Bryden, H.: Measuring the Atlantic Meridional Overturning Circulation at 26°N, *Progress in Oceanography*,
130, 91–111, doi:10.1016/j.pocean.2014.10.006, 2015.
- 696 Monterey, G., Levitus, S., *Climatological cycle of mixed layer depth in the world ocean*. U.S. government printing
office, NOAA NESDIS, Washington, DC, 5, pp., 1997.
- 698 Olbers, D. and Eden, C.: A Closure for Internal Wave–Mean Flow Interaction. Part I: Energy Conversion, *Journal of*
Physical Oceanography, 47(6), 1389–1401, doi:10.1175/jpo-d-16-0054.1, 2017.
- 700 Pacanowski, R. C. and Philander, S. G. H.: Parameterization of Vertical Mixing in Numerical Models of Tropical
Oceans, *Journal of Physical Oceanography*, 11(11), 1443–1451, doi:10.1175/1520-
702 0485(1981)011<1443:povmin>2.0.co;2, 1981.
- Petersen, M. R., Jacobsen, D. W., Ringler, T. D., Hecht, M. W. and Maltrud, M. E.: Evaluation of the arbitrary
704 Lagrangian–Eulerian vertical coordinate method in the MPAS-Ocean model, *Ocean Modelling*, 86, 93–113,
doi:10.1016/j.ocemod.2014.12.004, 2015.
- 706 Pollmann, F., Eden, C. and Olbers, D.: Evaluating the Global Internal Wave Model IDEMIX Using Finestructure
Methods, *Journal of Physical Oceanography*, 47(9), 2267–2289, doi:10.1175/jpo-d-16-0204.1, 2017.
- 708 Prims, O. T., Castrillo, M., Acosta, M. C., Mula-Valls, O., Lorente, A. S., Serradell, K., Cortés, A. and Doblaz-Reyes,
F. J.: Finding, analysing and solving MPI communication bottlenecks in Earth System models, *Journal of*
710 *Computational Science*, doi:10.1016/j.jocs.2018.04.015, 2018.
- Rackow, T., Goessling, H. F., Jung, T., Sidorenko, D., Semmler, T., Barbi, D. and Handorf, D.: Towards multi-
712 resolution global climate modeling with ECHAM6-FESOM. Part II: climate variability, *Climate Dynamics*,
50(7-8), 2369–2394, doi:10.1007/s00382-016-3192-6, 2016.
- 714 Redi, M. H.: Oceanic Isopycnal Mixing by Coordinate Rotation, *Journal of Physical Oceanography*, 12(10), 1154–1158,
doi:10.1175/1520-0485(1982)012<1154:oimbc>2.0.co;2, 1982.
- 716 Ringler, T., Petersen, M., Higdon, R. L., Jacobsen, D., Jones, P. W. and Maltrud, M.: A multi- resolution approach to
global ocean modeling, *Ocean Modelling*, 69, 211–232, doi:10.1016/j.ocemod.2013.04.010, 2013.
- 718 Scholz, P., Kieke, D., Lohmann, G., Ionita, M. and Rhein, M.: Evaluation of Labrador Sea Water formation in a global
Finite-Element Sea-Ice Ocean Model setup, based on a comparison with observational data, *Journal of*
720 *Geophysical Research: Oceans*, 119(3), 1644–1667, doi:10.1002/2013jc009232, 2014.
- Sein, D. V., Danilov, S., Biastoch, A., Durgadoo, J. V., Sidorenko, D., Harig, S. and Wang, Q.: Designing variable
722 ocean model resolution based on the observed ocean variability, *Journal of Advances in Modeling Earth*



- Systems, 8(2), 904–916, doi:10.1002/2016ms000650, 2016.
- 724 Sein, D. V., Koldunov, N. V., Danilov, S., Wang, Q., Sidorenko, D., Fast, I., Rackow, T., Cabos, W. and Jung, T.:
Ocean Modeling on a Mesh With Resolution Following the Local Rossby Radius, *Journal of Advances in*
726 *Modeling Earth Systems*, 9(7), 2601–2614, doi:10.1002/2017ms001099, 2017.
- Sein, D. V., Koldunov, N. V., Danilov, S., Sidorenko, D., Wekerle, C., Cabos, W., Rackow, T., Scholz, P., Semmler, T.,
728 Wang, Q. and Jung, T.: The Relative Influence of Atmospheric and Oceanic Model Resolution on the
Circulation of the North Atlantic Ocean in a Coupled Climate Model, *Journal of Advances in Modeling Earth*
730 *Systems*, 10(8), 2026–2041, doi:10.1029/2018ms001327, 2018.
- Shi, X. and Lohmann, G.: Simulated response of the mid-Holocene Atlantic meridional overturning circulation in
732 ECHAM6-FESOM/MPIOM, *Journal of Geophysical Research: Oceans*, 121(8), 6444–6469,
doi:10.1002/2015jc011584, 2016.
- 734 Sidorenko, D., Koldunov, N. V., Wang, Q., Danilov, S., Goessling, H. F., Gurses, O., Scholz, P., Sein, D. V., Volodin,
E., Wekerle, C. and Jung, T.: Influence of a Salt Plume Parameterization in a Coupled Climate Model, *Journal of*
736 *Advances in Modeling Earth Systems*, 10(9), 2357–2373, doi:10.1029/2018ms001291, 2018.
- Sidorenko, D., Danilov, S., Wang, Q., Huerta-Casas, A. and Schröter, J.: On computing transports in finite-element
738 models, *Ocean Modelling*, 28(1-3), 60–65, doi:10.1016/j.ocemod.2008.09.001, 2009.
- Sidorenko, D., Rackow, T., Jung, T., Semmler, T., Barbi, D., Danilov, S., Dethloff, K., Dorn, W., Fieg, K., Goessling,
740 H. F., Handorf, D., Harig, S., Hiller, W., Juricke, S., Losch, M., Schröter, J., Sein, D. V. and Wang, Q.: Towards
multi-resolution global climate modeling with ECHAM6-FESOM. Part I: model formulation and mean climate,
742 *Climate Dynamics*, 44(3-4), 757–780, doi:10.1007/s00382-014-2290-6, 2014.
- Sidorenko, D., Wang, Q., Danilov, S. and Schröter, J.: FESOM under coordinated ocean-ice reference experiment
744 forcing, *Ocean Dynamics*, 61(7), 881–890, doi:10.1007/s10236-011-0406-7, 2011.
- Smeed, D. A., Mccarthy, G. D., Cunningham, S. A., Frajka-Williams, E., Rayner, D., Johns, W. E., Meinen, C. S.,
746 Baringer, M. O., Moat, B. I., Duchez, A. and Bryden, H. L.: Observed decline of the Atlantic meridional
overturning circulation 2004–2012, *Ocean Science*, 10(1), 29–38, doi:10.5194/os-10-29-2014, 2014.
- 748 Shchepetkin, A. F.: An adaptive, Courant-number-dependent implicit scheme for vertical advection in oceanic
modeling, *Ocean Modelling*, 91, 38–69, 2015.
- 750 Steele, M., Morley, R. and Ermold, W.: PHC: A Global Ocean Hydrography with a High-Quality Arctic Ocean, *Journal*
of Climate, 14(9), 2079–2087, doi:10.1175/1520-0442(2001)014<2079:pagoHW>2.0.CO;2, 2001.
- 752 Storch, J.-S. V., Eden, C., Fast, I., Haak, H., Hernández-Deckers, D., Maier-Reimer, E., Marotzke, J. and Stammer, D.:
An Estimate of the Lorenz Energy Cycle for the World Ocean Based on the STORM/NCEP Simulation, *Journal*
754 *of Physical Oceanography*, 42(12), 2185–2205, doi:10.1175/jpo-d-12-079.1, 2012.
- Timmermann, R., Danilov, S., Schröter, J., Böning, C., Sidorenko, D. and Rollenhagen, K.: Ocean circulation and sea
756 ice distribution in a finite element global sea ice–ocean model, *Ocean Modelling*, 27(3-4), 114–129, doi:10.1016/
j.ocemod.2008.10.009, 2009.
- 758 Wang, Q., Danilov, S., Sidorenko, D., Timmermann, R., Wekerle, C., Wang, X., Jung, T. and Schröter, J.: The Finite
Element Sea Ice-Ocean Model (FESOM) v.1.4: formulation of an ocean general circulation model, *Geoscientific*
760 *Model Development*, 7(2), 663–693, doi:10.5194/gmd-7-663-2014, 2014.
- Wang, Q., Danilov, S. and Schröter, J.: Finite element ocean circulation model based on triangular prismatic elements,



- 762 with application in studying the effect of topography representation, *Journal of Geophysical Research*, 113(C5),
doi:10.1029/2007jc004482, 2008.
- 764 Wang, Q., Danilov, S., Jung, T., Kaleschke, L. and Wernecke, A.: Sea ice leads in the Arctic Ocean: Model assessment,
interannual variability and trends, *Geophysical Research Letters*, 43(13), 7019–7027,
766 doi:10.1002/2016gl068696, 2016.
- Wang, Q., Ilicak, M., Gerdes, R., Drange, H., Aksenov, Y., Bailey, D. A., Bentsen, M., Biastoch, A., Bozec, A.,
768 Böning, C., Cassou, C., Chassignet, E., Coward, A. C., Curry, B., Danabasoglu, G., Danilov, S., Fernandez, E.,
Fogli, P. G., Fujii, Y., Griffies, S. M., Iovino, D., Jahn, A., Jung, T., Large, W. G., Lee, C., Lique, C., Lu, J.,
770 Masina, S., Nurser, A. G., Rabe, B., Roth, C., Méliá, D. S. Y., Samuels, B. L., Spence, P., Tsujino, H., Valcke,
S., Voldoire, A., Wang, X. and Yeager, S. G.: An assessment of the Arctic Ocean in a suite of interannual
772 CORE-II simulations. Part I: Sea ice and solid freshwater, *Ocean Modelling*, 99, 110–132,
doi:10.1016/j.ocemod.2015.12.008, 2016a.
- 774 Wang, Q., Ilicak, M., Gerdes, R., Drange, H., Aksenov, Y., Bailey, D. A., Bentsen, M., Biastoch, A., Bozec, A.,
Böning, C., Cassou, C., Chassignet, E., Coward, A. C., Curry, B., Danabasoglu, G., Danilov, S., Fernandez, E.,
776 Fogli, P. G., Fujii, Y., Griffies, S. M., Iovino, D., Jahn, A., Jung, T., Large, W. G., Lee, C., Lique, C., Lu, J.,
Masina, S., Nurser, A. G., Rabe, B., Roth, C., Méliá, D. S. Y., Samuels, B. L., Spence, P., Tsujino, H., Valcke,
778 S., Voldoire, A., Wang, X. and Yeager, S. G.: An assessment of the Arctic Ocean in a suite of interannual
CORE-II simulations. Part II: Liquid freshwater, *Ocean Modelling*, 99, 86–109,
780 doi:10.1016/j.ocemod.2015.12.009, 2016b.
- Wang, Q., Wekerle, C., Danilov, S., Wang, X. and Jung, T.: A 4.5 km resolution Arctic Ocean simulation with the
782 global multi-resolution model FESOM1.4, *Geoscientific Model Development*, 11, 1229–1255, 2018a.
- Wang, Q., Wekerle, C., Danilov, S., Koldunov, N., Sidorenko, D., Sein, D., Rabe, B. and Jung, T.: Arctic Sea Ice
784 Decline Significantly Contributed to the Unprecedented Liquid Freshwater Accumulation in the Beaufort Gyre
of the Arctic Ocean, *Geophysical Research Letters*, 45, 4956–4964, 2018b.
- 786 Wang, Q., Marshall, J., Scott, J., Meneghello, G., Danilov, S. and Jung, T.: On the feedback of ice-ocean stress coupling
from geostrophic currents in an anticyclonic wind regime over the Beaufort Gyre, *J. Physical Oceanography*,
788 <https://doi.org/10.1175/JPO-D-18-0185.1>, accepted, 2019a.
- Wang, Q., Wekerle, C., Danilov, S., Sidorenko, D., Koldunov, N., Sein, D., Rabe, B. and Jung, T.: Recent Sea Ice
790 Decline Did Not Significantly Increase the Total Liquid Freshwater Content of the Arctic Ocean, *J. Climate*, 32,
15–32, 2019b.
- 792 Wekerle, C., Wang, Q., Danilov, S., Schourup-Kristensen, V., Appen, W.-J. V. and Jung, T.: Atlantic Water in the
Nordic Seas: Locally eddy-permitting ocean simulation in a global setup, *Journal of Geophysical Research:
794 Oceans*, 122(2), 914–940, doi:10.1002/2016jc012121, 2017.
- White, L., Deleersnijder, E. and Legat, V.: A three-dimensional unstructured mesh finite element shallow-water model,
796 with application to the flows around an island and in a wind-driven, elongated basin, *Ocean Modelling*, 22(1–2),
26–47, doi:10.1016/j.ocemod.2008.01.001, 2008.
- 798 Wunsch, C. and Ferrari, R.: Vertical Mixing, Energy, And The General Circulation Of The Oceans, *Annual Review of
Fluid Mechanics*, 36(1), 281–314, doi:10.1146/annurev.fluid.36.050802.122121, 2004.



Figures

802

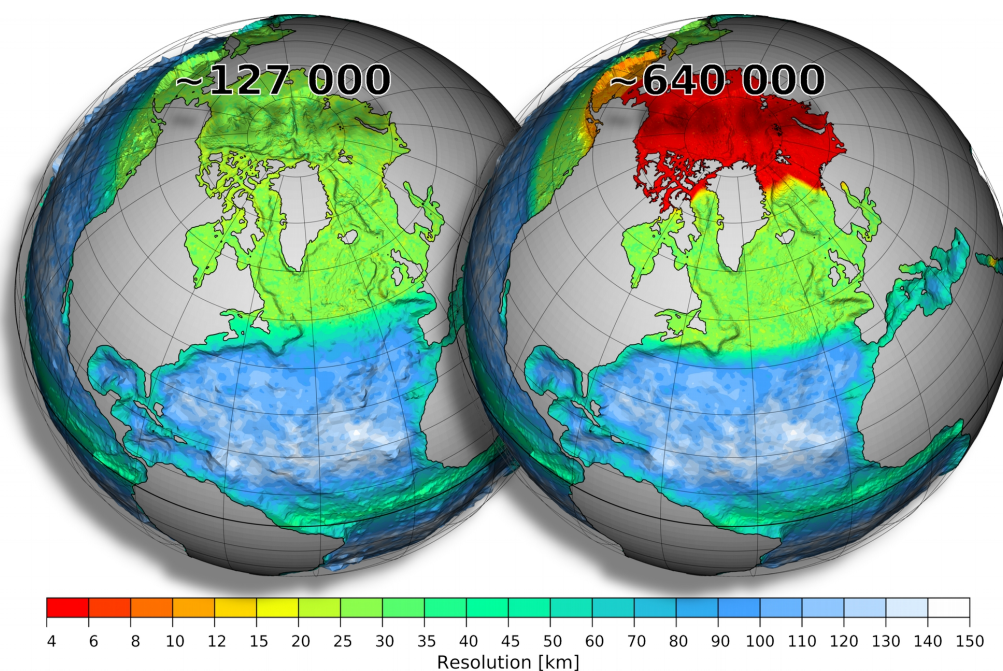


Figure 1: Horizontal resolution of mesh configurations used in this study: The smaller reference (left, ~127 000 surface vertices) and larger medium-sized (right, ~640 000 surface vertices) mesh. The two meshes have the same resolution (nominal resolution of 1° in most parts of the global ocean, ~ 25 km north of 50°N , $\sim 1/3^\circ$ at the equator) except for the Arctic Ocean and Bering Sea. There the medium sized mesh has an increased resolution of 4.5 km and 10 km for the Arctic Ocean and Bering Sea, respectively.

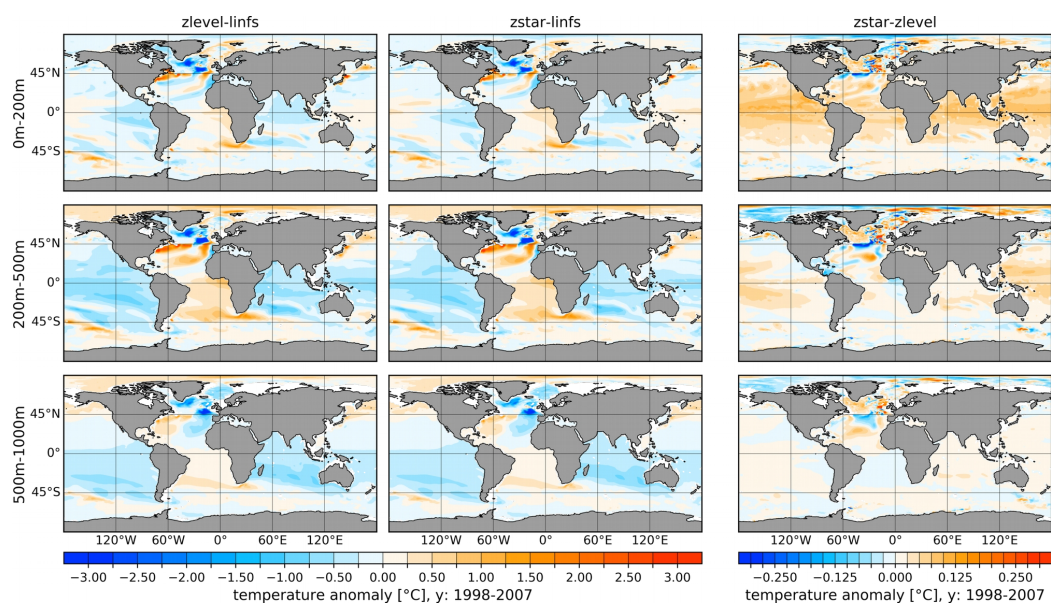


Figure 2: Temperature anomalies of the full free surface simulations with respect to the linear free surface simulation: zlevel minus linfs (left column) and zstar minus linfs (middle column). The right column shows the temperature difference between the two full free surface simulations (zstar minus zlevel). From top to bottom the three rows show the results for three different depth ranges: 0-200 m, 200-500 m and 500-1000 m. Averages over the time period 1998-2007 are shown. Note that different color scales are used.

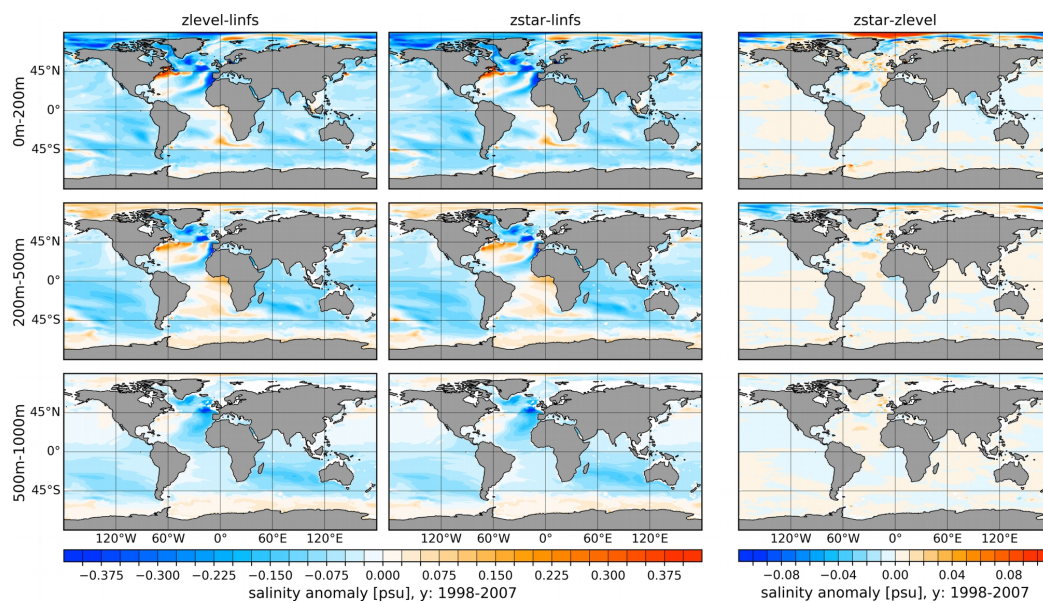


Figure 3: Same as Fig. 2 but for salinity

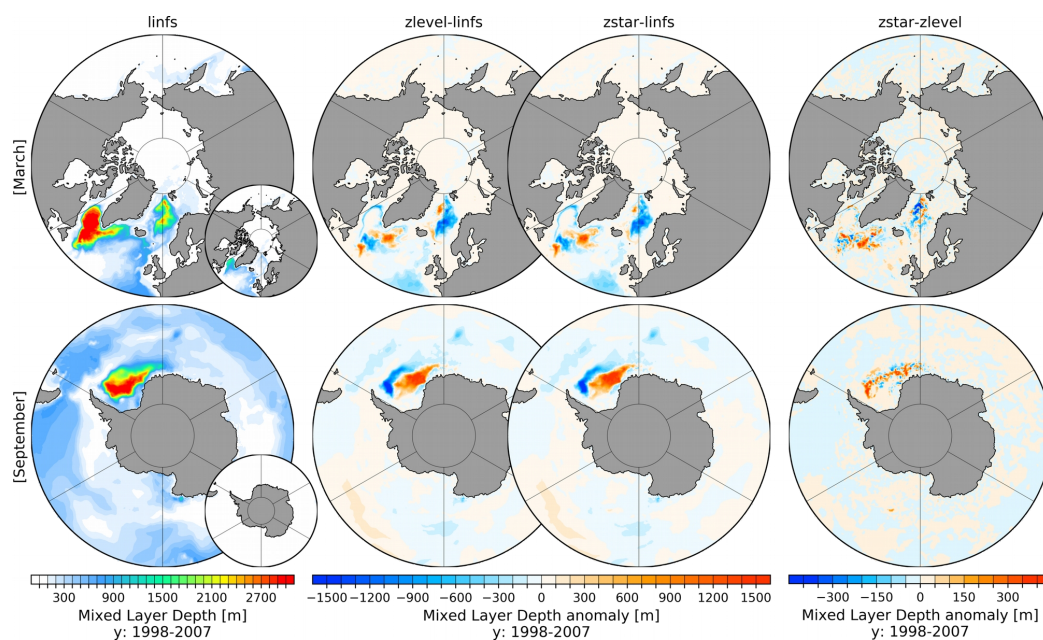


Figure 4: March (upper row) and September (lower row) mixed layer depth (MLD, definition after Monterey and Levitus, 1997) for the linear free surface case (lins, 1st column) averaged for the time interval 1998-2007. 2nd. and 3rd. column show the anomalous MLD for the full free surface modes zlevel (2nd. column) and zstar (3rd. column) with respect to the lins mode. The 4th. column presents the anomalous MLD between the two full free surface modes (zstar-minus zlevel). Small inset plot shows the MLD after the definition of Large et al., 1997.

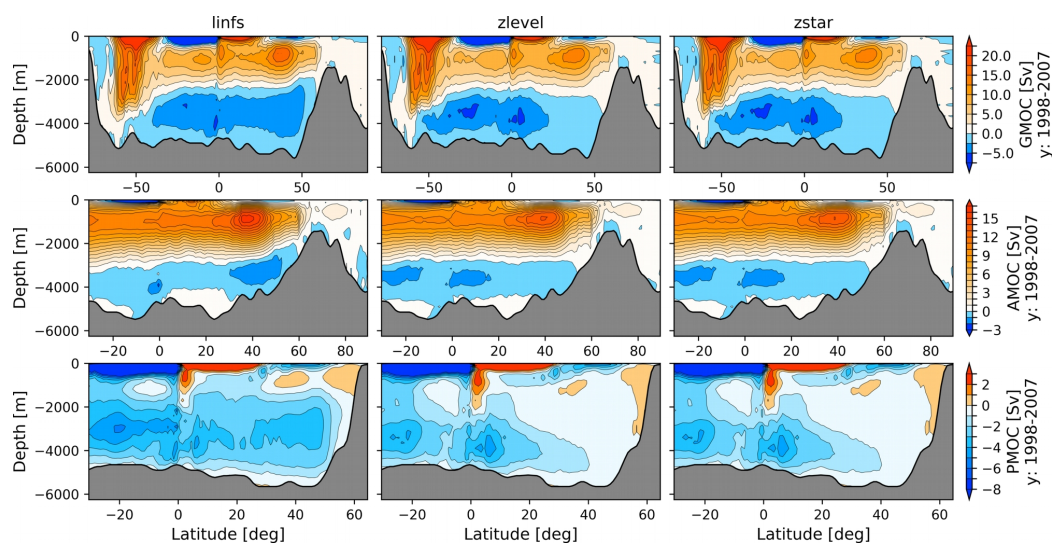


Figure 5: Global (GMOC, upper row), Atlantic (AMOC, middle row) and Indo-Pacific (PMOC, lower row) Meridional Overturning Circulation for the linear free surface formulation lins (left column), and the full free surface zlevel option (middle column) and zstar option (right column). The average over the time period 1998-2007 is shown. Note that different color ranges are used.

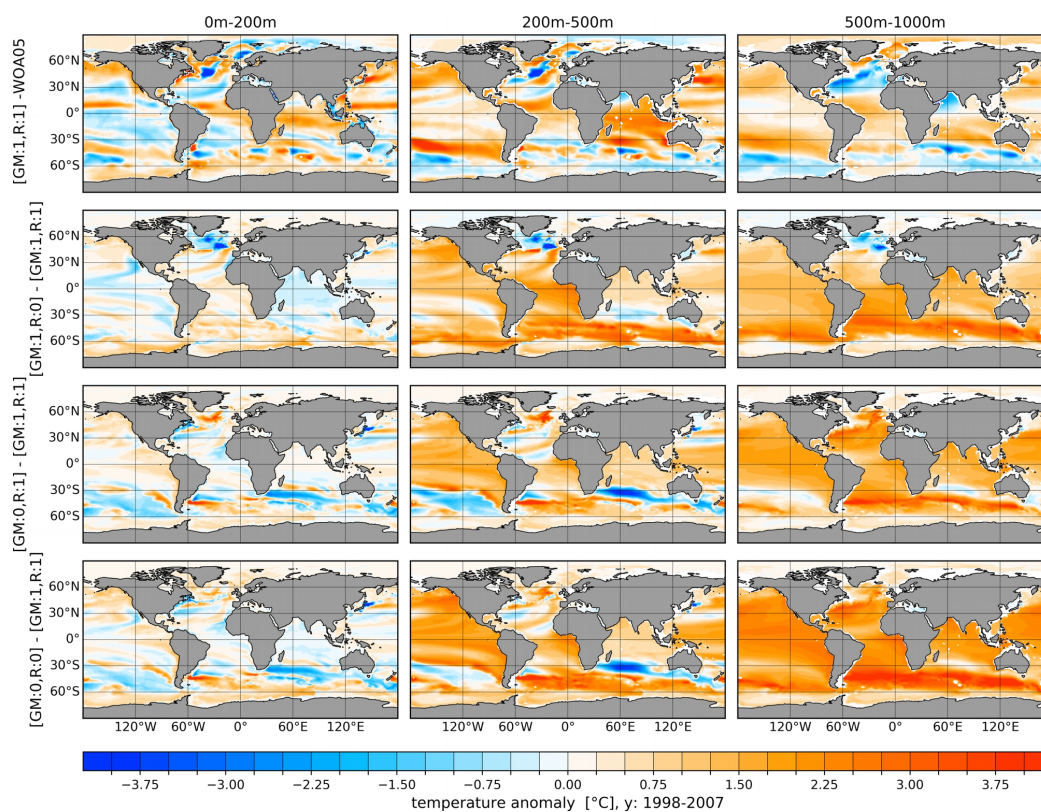


Figure 6: First row: Temperature biases in the reference simulation with respect to the World Ocean Atlas 2005 (WOA05, Locarnini et al., 2006; Antonov et al., 2006) climatology for three different depth ranges: 0-200 m (left), 200-500 m (middle) and 500-1000 m (right). In the reference simulation both the GM and Redi diffusion parameterizations are switched on (:1). Another three rows show the temperature differences between sensitivity runs and the reference run. The second row shows the impact when only the Redi diffusivity is switched off (:0), the third row when only GM is switched off, and the fourth row when both of them are switched off. The average over the period 1998-2007 is shown.

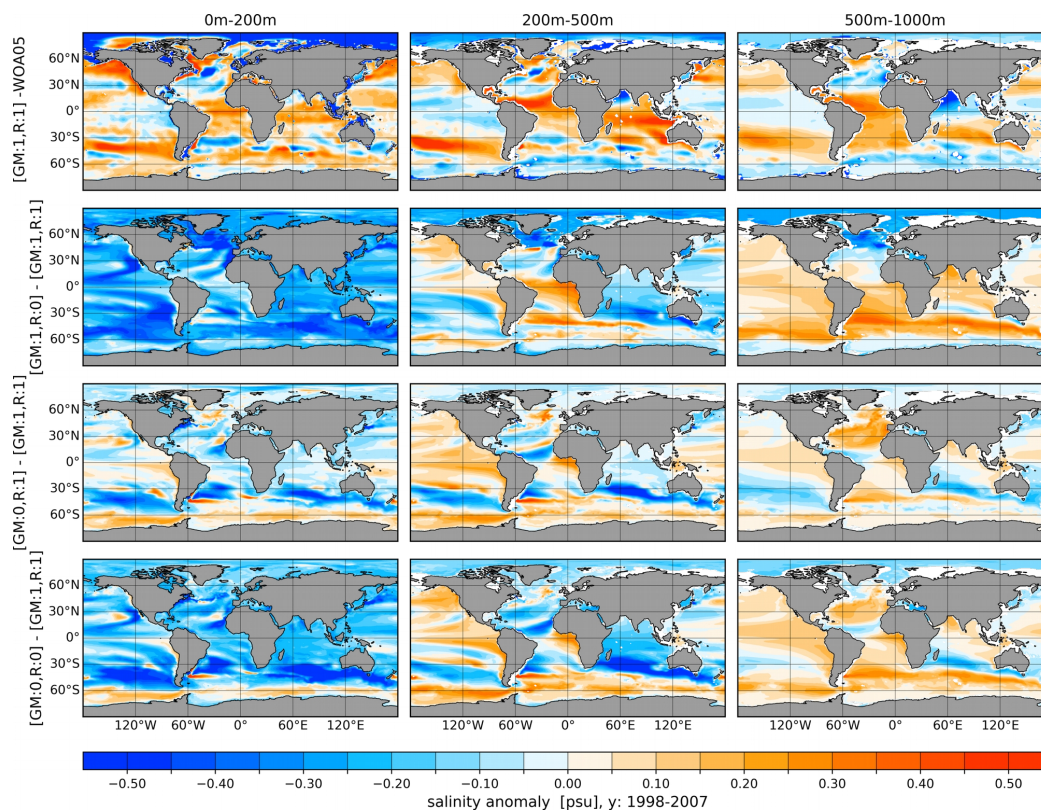


Figure 7: Same as Fig. 6 but for salinity

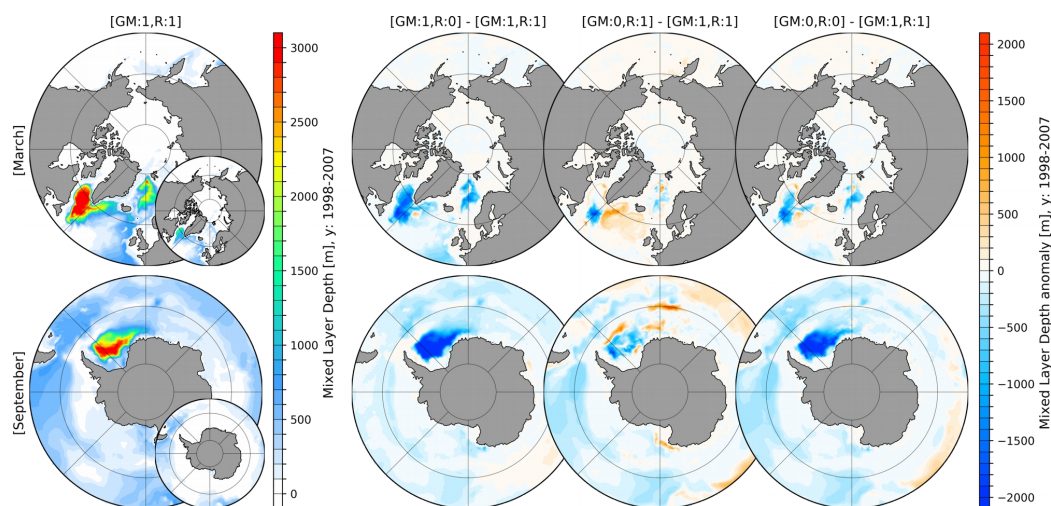


Figure 8: 1st column: March (upper row) and September (lower row) mean mixed layer depth (MLD, definition after Monterey and Levitus, 1997) for the simulation with switched on (:1) Gent McWilliams parameterisation (GM) and Redi Diffusion (R) averaged over the period 1998-2007. 2nd-4th column: anomalous MLD of simulations with either switched off (:0) GM or R, or both switched off with respect to the control simulation where GM and R are both switched on. Small inset plots shows the MLD after the definition of Large et al. (1997).

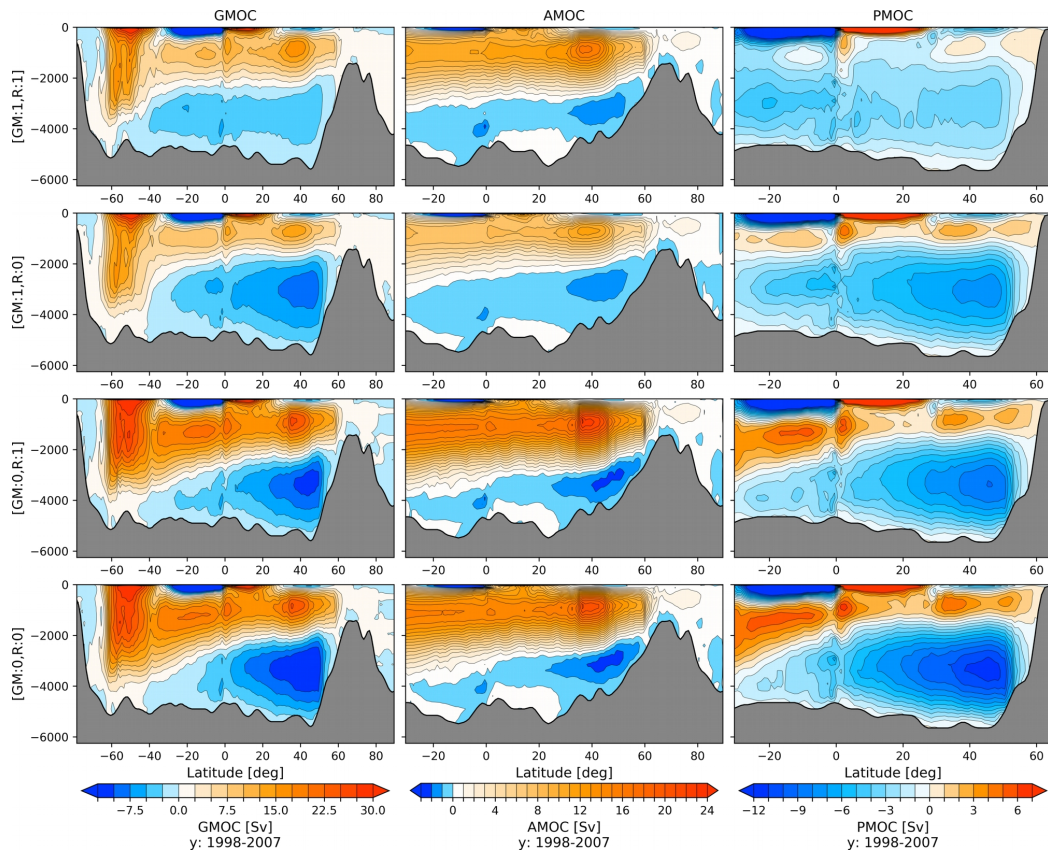


Figure 9: Global (GMOC, 1st. column), Atlantic (AMOC, 2nd. column) and Indo-Pacific (PMOC, 3rd. column) Meridional Overturning Circulation averaged for the time period 1998-2007 for: (1st row) the reference run with switched on GM and Redi (:1), (2nd row) the run with switched off Redi diffusivity (:0), (3rd row) GM switched off, and (4th row) both parameterizations switched off. Note different color ranges are used.



820

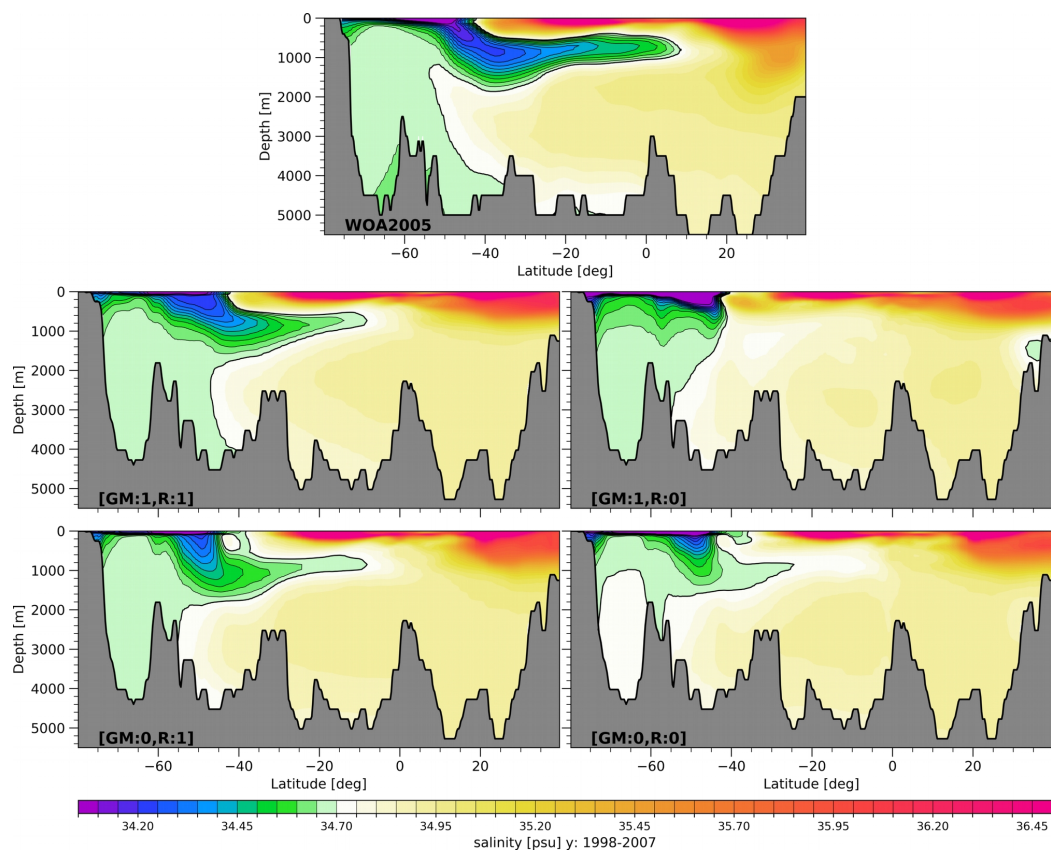


Figure 10: (upper) Mean Salinity in a vertical section from -30°W , -80°S to -30°W , 40°N , derived from the World Ocean Atlas 2005 (WOA05, Locarnini et al., 2006; Antonov et al., 2006) annual climatology. The other four panels show the results from model simulations: (upper left) the reference run with switched on GM and Redi, (upper right) the run with Redi diffusivity set to zero, (lower left) the run with GM switched off, and (lower right) both parameterizations switched off. Contour lines highlight the spreading of Antarctic Intermediate Water (<34.70 psu) northward.

822

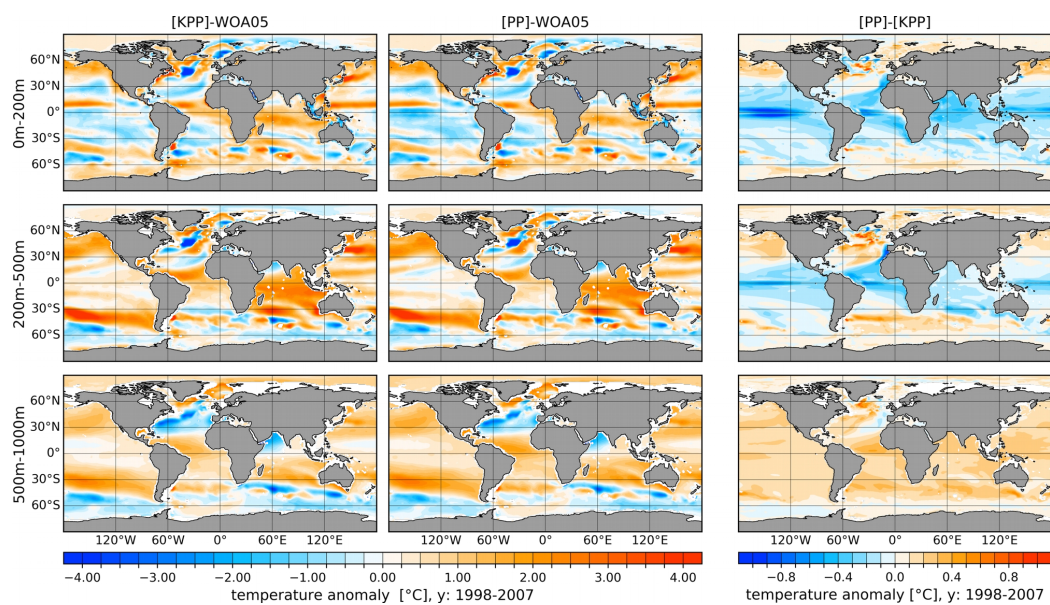


Figure 11: Temperature biases in model simulations referenced to the World Ocean Atlas 2005 (WOA05, Locarnini et al., 2006; Antonov et al., 2006) averaged over the period 1998-2007 for: (left column) the simulation with the KPP vertical mixing scheme and (center column) the simulation with the PP mixing scheme. The right column shows the difference between the two simulations. From top to bottom the panels show the vertically averaged fields for the depth ranges of 0-200 m (upper row), 200-500 m (middle row) and 500-1000 m (lower row).

824

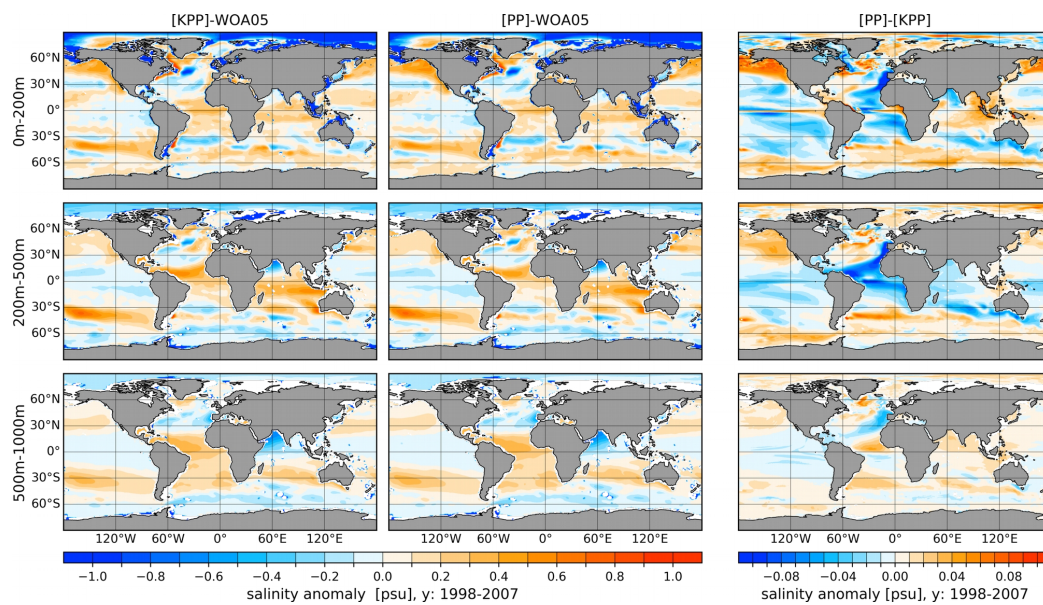


Figure 12: Same as Fig. 11 but for salinity.

826

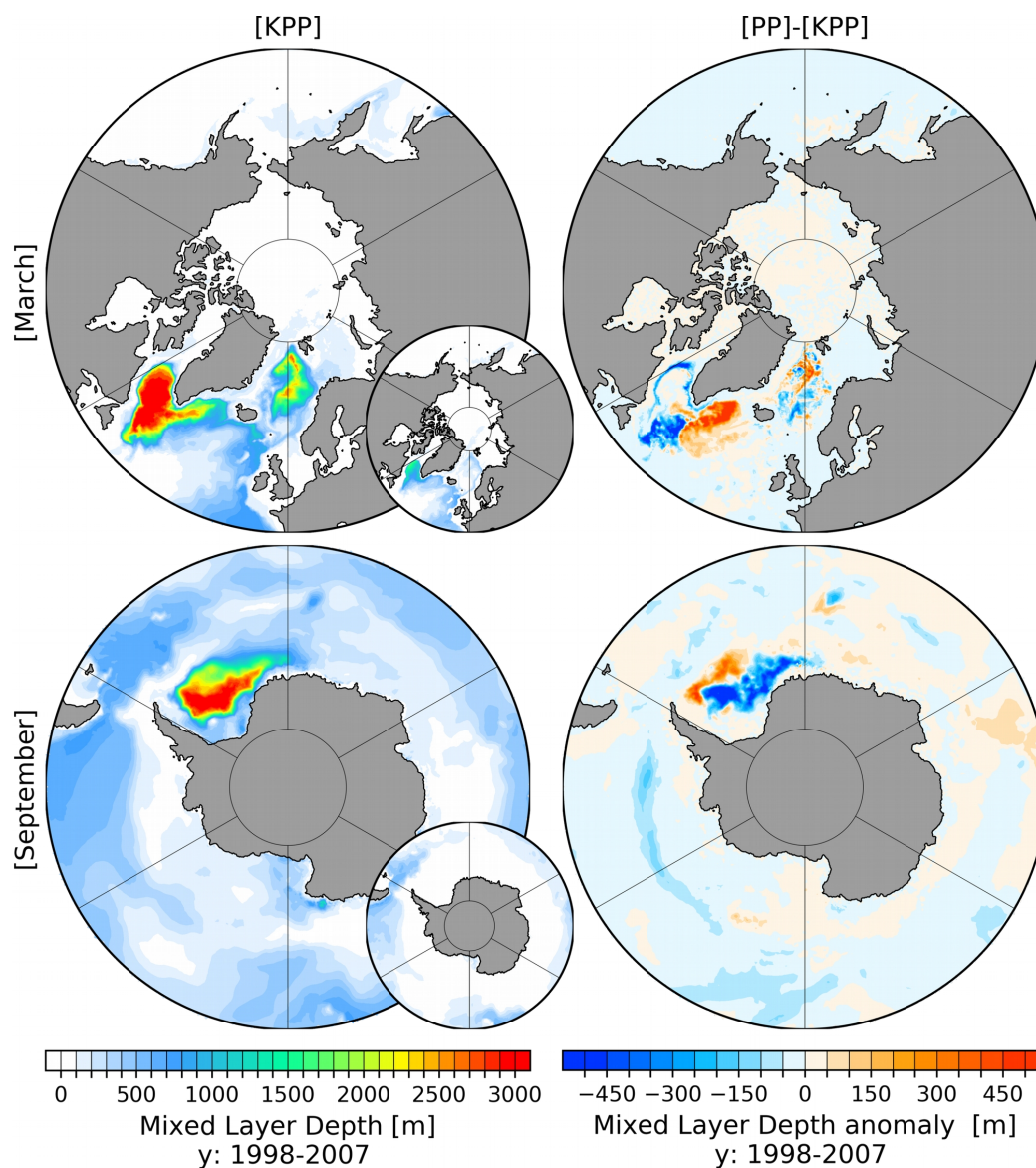


Figure 13: March (upper row) and September (lower row) mean mixed layer depth (MLD, definition after Monterey and Levitus, 1997) for the simulation with KPP (left column) and PP (right column) vertical mixing averaged over the period 1998-2007. Small inset plots shows the MLD after the definition of Large et al. (1997).

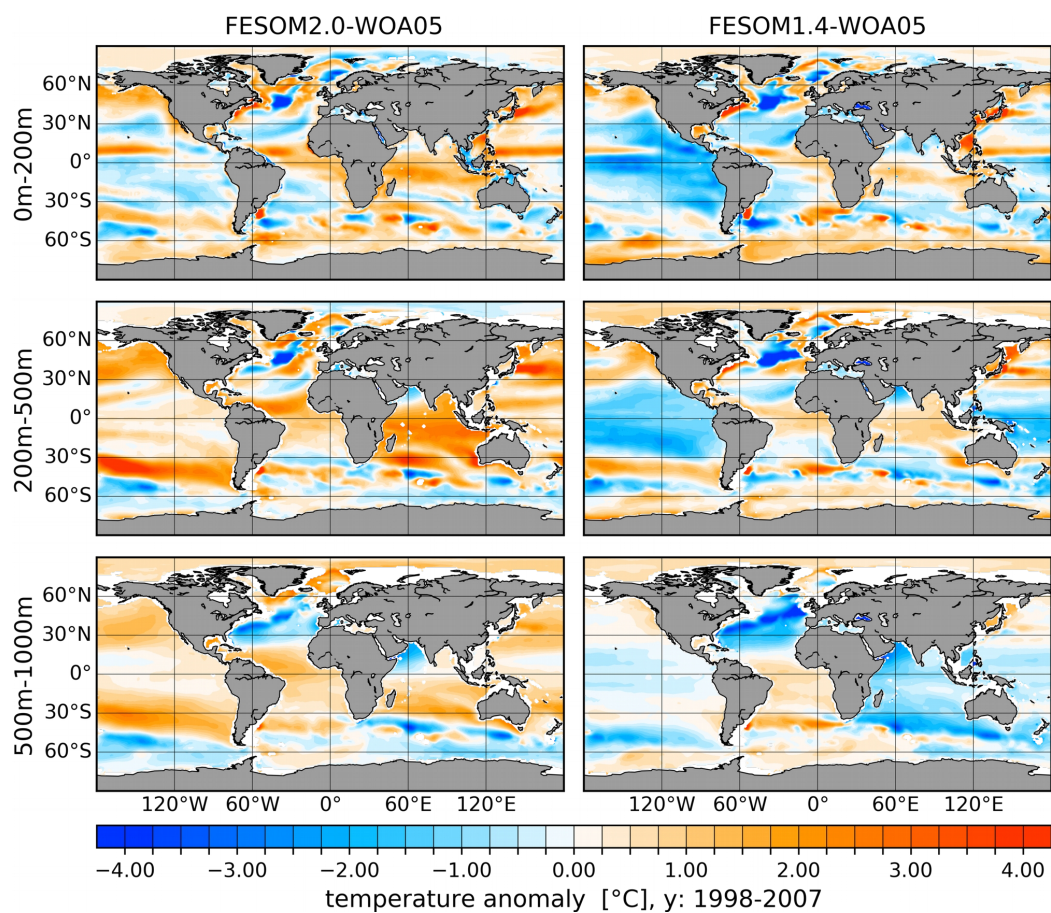


Figure 14: Temperature biases referenced to the World Ocean Atlas 2005 (WOA05, Locarnini et al., 2006; Antonov et al., 2006) climatology for FESOM2.0 (left column) and FESOM1.4 (right column) Model results are averaged over the period 1998-2007. From top to bottom averages over three depth ranges are shown: 0-200 m (upper row), 200-500 m (middle row) and 500-1000 m (lower row).

830

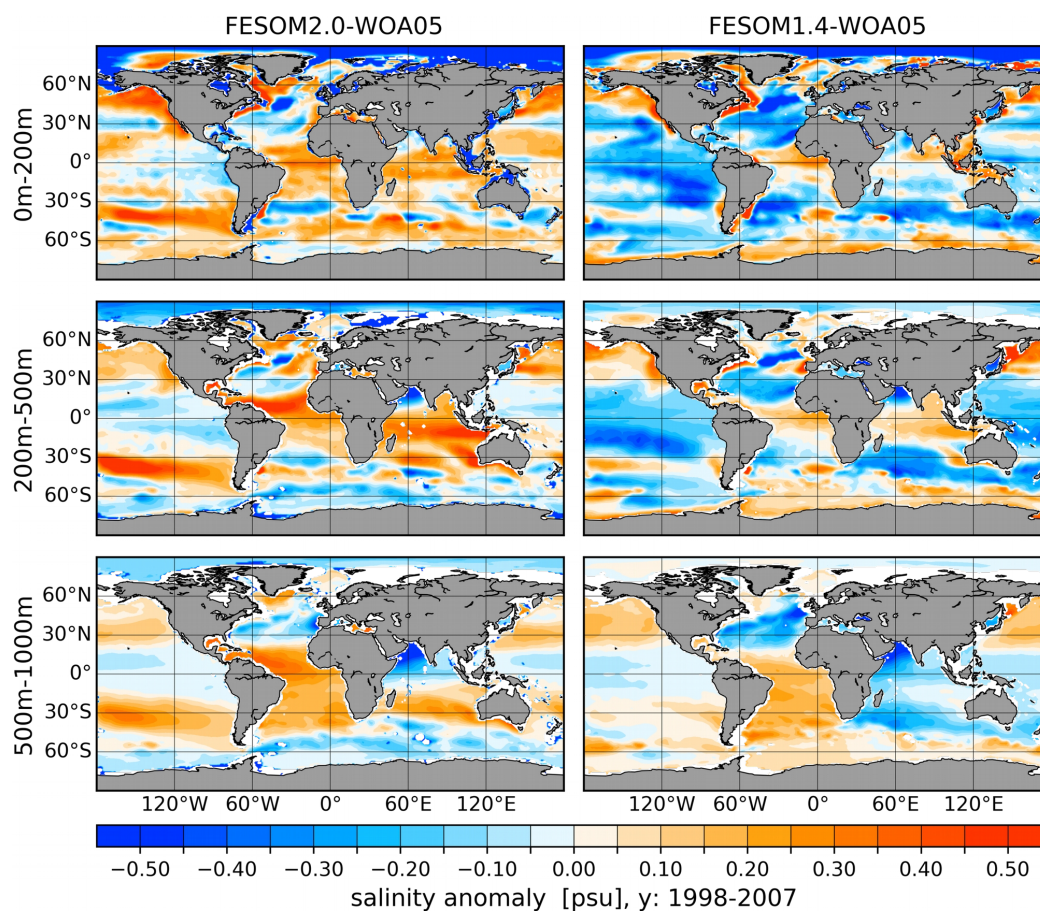


Figure 15: Same as Fig. 14 but for salinity.

832

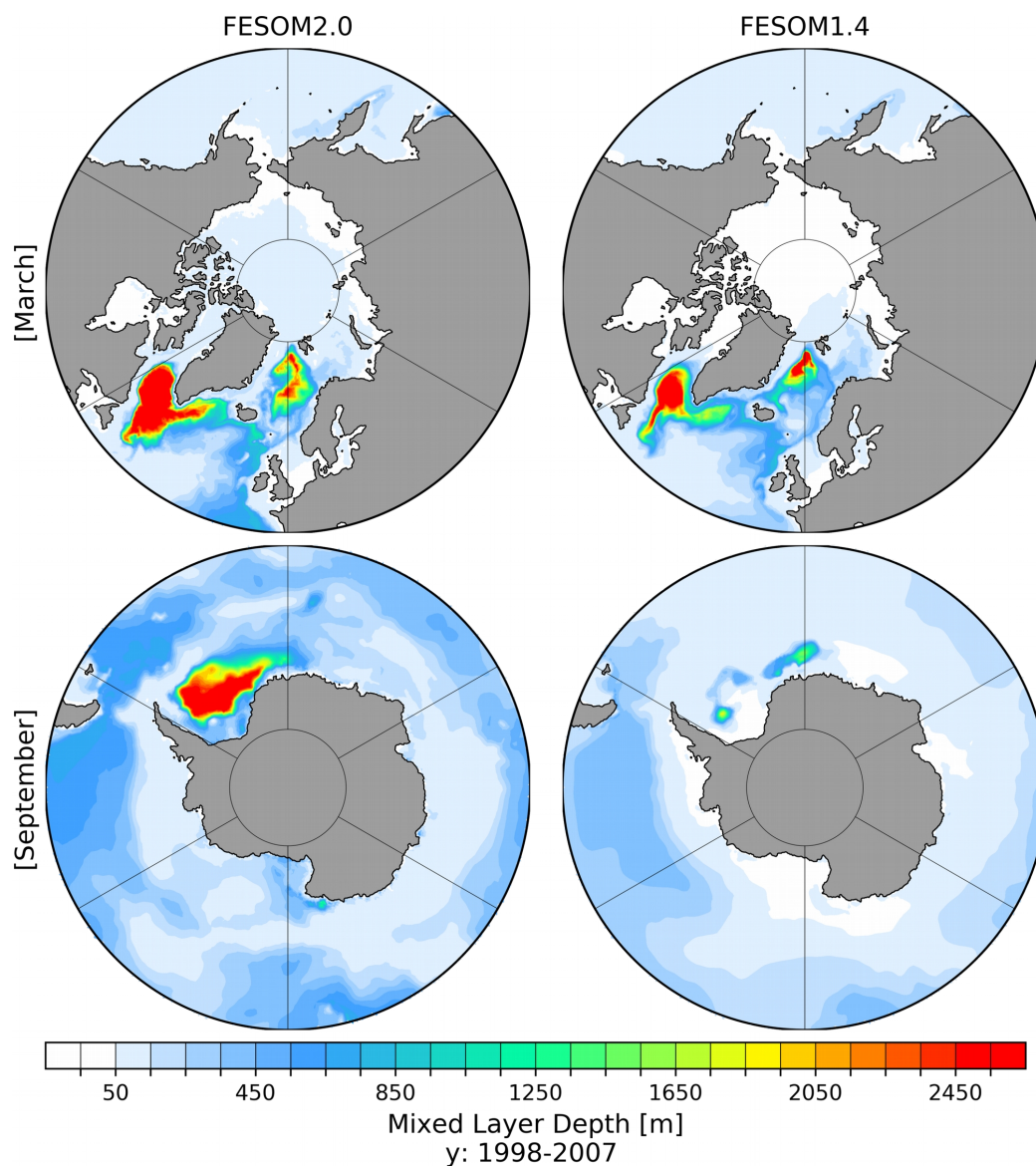


Figure 16: March (upper row) and September (lower row) mean mixed layer depth (MLD, definition after Monterey and Levitus, 1997) averaged over the period 1998-2007 of a FESOM2.0 (left column, GM, Redi and KPP) and FESOM1.4 (right column, GM, Redi and KPP) reference simulation.

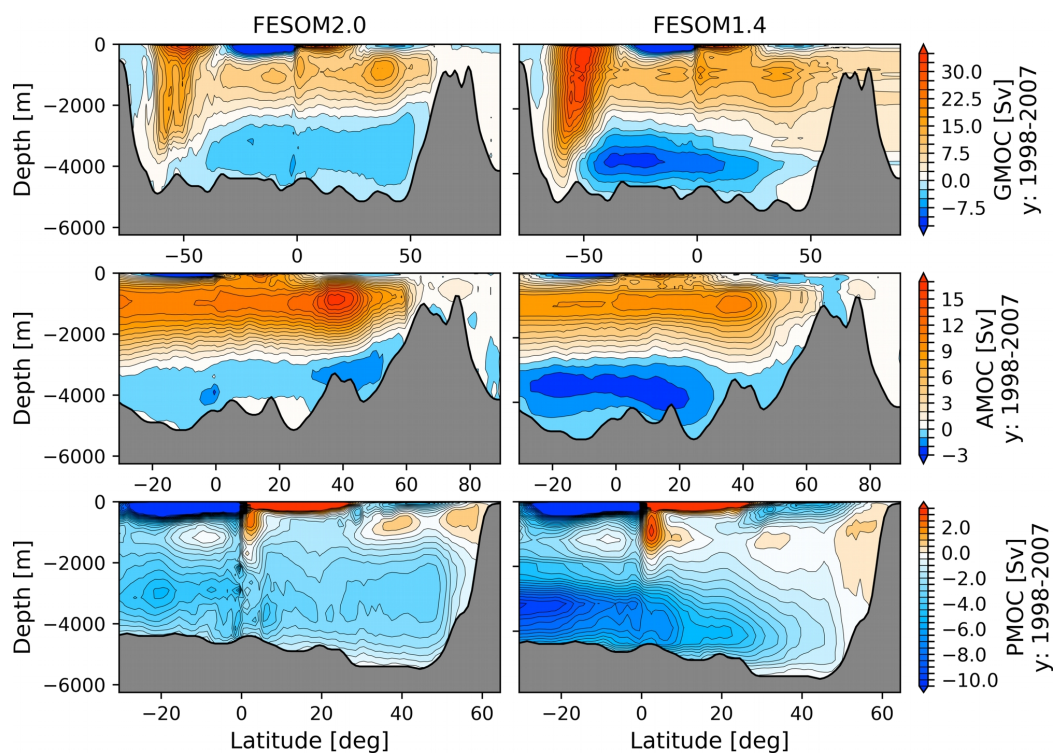


Figure 17: Global (GMOC, upper row), Atlantic (AMOC, middle row) and Indo-Pacific (PMOC, lower row) Meridional Overturning Circulation averaged for the time period 1998-2007: FESOM2.0 (left column) and FESOM1.4 (right column).

836

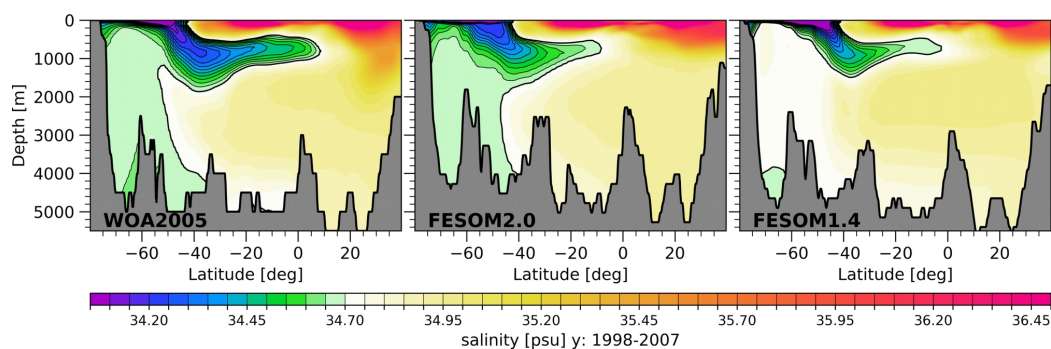


Figure 18: Mean Salinity in the vertical section from -30°W , -80°S to -30°W , 40°N : World Ocean Atlas 2005 (WOA05, Locarnini et al., 2006; Antonov et al., 2006) annual climatology (left), FESOM2.0 (middle) and FESOM1.4 (right). Model results are averaged for the period 1998-2007. Contour lines highlight the spreading of Antarctic intermediate water (<34.70 psu) northward.

838

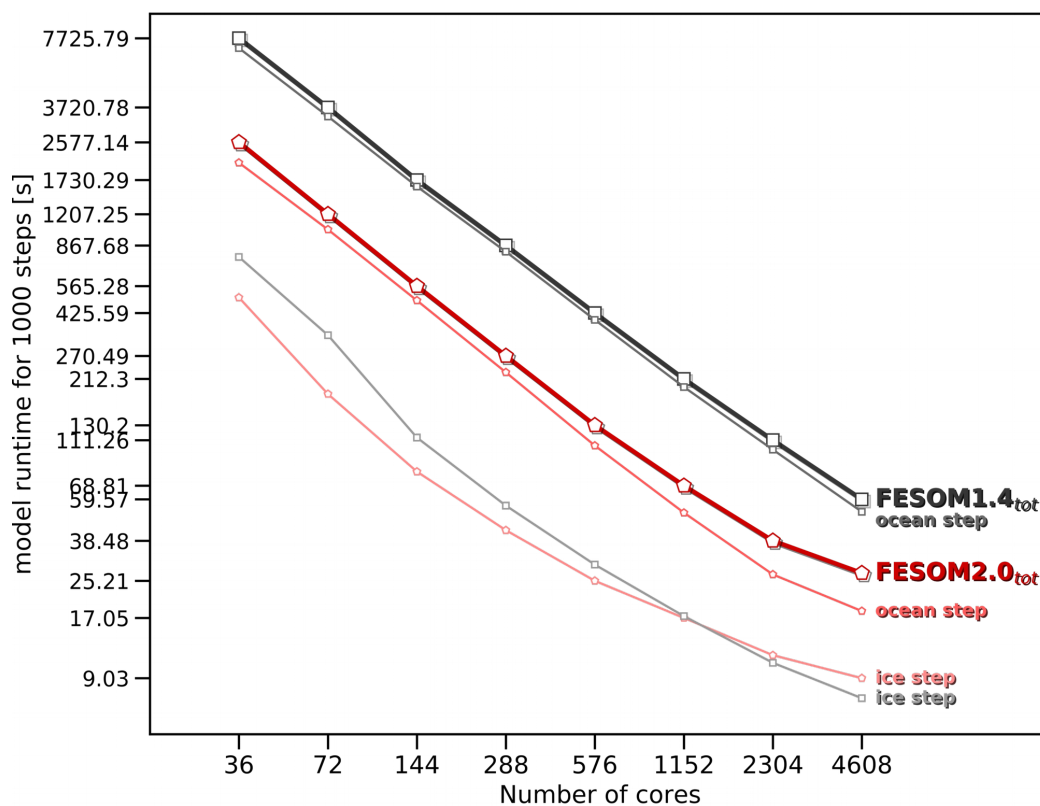


Figure 19: Scaling performance of FESOM1.4 and FESOM2.0 on different number of cores for the medium-size mesh configuration (see Fig. 1 right) with ~0.64M surface vertices.

840

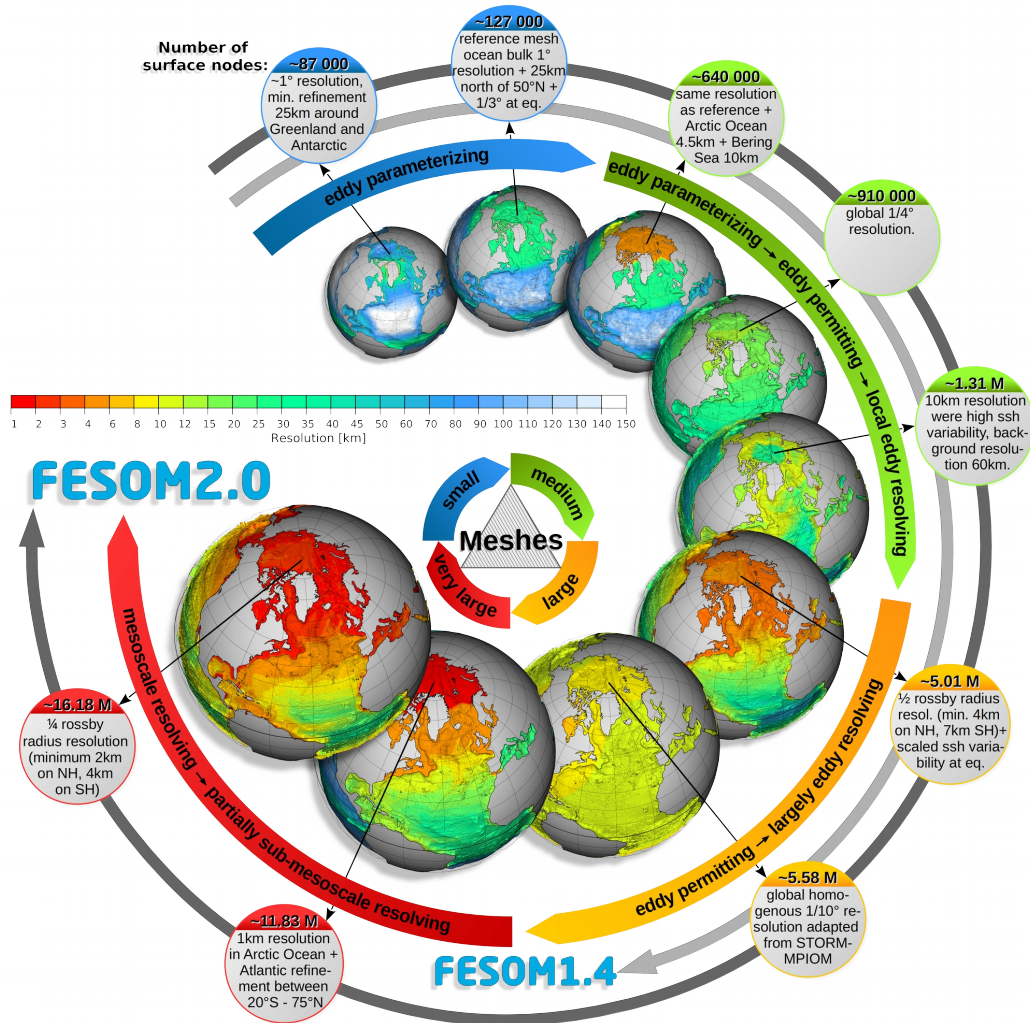


Figure 20: Schematic representation of mesh applicability of FESOM1.4 and FESOM2.0.

842